Nonlinear 3D Path Following Control of a Fixed-Wing Aircraft based on Acceleration Control

A. Galffy*, M. Böck, A. Kugi

Automation and Control Institute, Vienna University of Technology, Gußhausstraße 27-29, 1040 Vienna, Austria

Abstract

This paper focuses on the design of a novel path following control concept for fixed-wing aircraft, which systematically incorporates the nonlinearities of the flight dynamics. By introducing an acceleration based inner loop control, feedforward acceleration demands of nonlinear 3D paths can be directly taken into account. Furthermore, the nonlinear effects of airspeed, orientation, and gravity are considered separately by implementing a cascaded design and feedback linearization. As a result, robust performance of the path following control is achieved even for wind speeds in the order of the aircraft's airspeed and path accelerations significantly higher than the gravitational acceleration. By further including direct lift control, a high-bandwidth vertical acceleration control is developed. Results of flight experiments show that the designed control concept is particularly beneficial in terms of the tracking performance for 3D paths, the incorporation of input constraints, the robustness against wind and turbulence effects, and the ease of implementation as well as the low computational complexity.

Keywords: 3D Path following, Fixed-wing aircraft, Feedback linearization, Acceleration control, Direct lift control
2010 MSC: 00-01, 99-00

1. Introduction

Path following control (PFC) aims at restricting the motion of an object to a specified path in space without time parameterization. Thus, PFC may be considered as a generalization of the time-based trajectory tracking concept, which may enhance the performance of control systems, see, e. g., Aguiar et al. (2008). Applied to aviation, following a flight path as primary control objective and considering the path speed as secondary objective is a well-established concept. As an example, instrument approach procedures for airliner and private airplanes are defined by paths in the 3D space with regard to radio navigational aids. The exact timing of the approach is secondary and significantly varies depending on the aircraft type and wind conditions. The accurate tracking of the authorized flight path as primary target is essential for collision avoidance based on sufficient spatial separation of the aircraft from terrain, infrastructure and other air traffic. In this context, being exposed to environmental disturbances like wind, gusts, and turbulence, PFC shows the potential to handle stronger disturbances compared to trajectory tracking methods. Effective disturbance rejection is particularly critical for the reliable operation of small-size aircraft, like UAVs and private aircraft. To this end, classical direct lift control can be considered to enhance

the suppression of turbulence and to improve the dynamic response of lift generation independently from orientation, see, e. g., Pinsker (1970).

This paper presents a cascaded design with an acceleration based inner loop control, feedback linearization, state control with pole placement, and SISO in-flight identification. Moreover, the concept is validated for 3D test paths with variable airspeeds. In contrast, a notable approach of recent research, Muniraj et al. (2017), is characterized by an integrated non-cascaded design with an orientation based inner control loop, a linear parameter varying (LPV) system corresponding to equilibrium state linearization, H_∞ control, and state-space identification. The validation is performed for 2D test paths with constant airspeed, whereas the control concept in principle also incorporates 3D paths. Other approaches are discussed in the work of Sujit et al. (2014), which compares different algorithms of PFC for fixed-wing UAVs to track straight lines and circular orbits with constant altitude and airspeed. Thereby, an overview of well-known PFC techniques like linear quadratic regulator (LQR), sliding mode control, model predictive control (MPC), backstepping control, adaptive control, and dynamic programming is given. Based on 6-DOF simulation models, a number of different algorithms, e. g., a nonlinear guidance logic in Park et al. (2007), vector-field-based PFC in Nelson et al. (2007), and LQR in Ratnoo et al. (2011) were investigated. The nonlinear guidance logic is known for being implemented in the open-source software Ardupilot (2018) and

---

*Corresponding author. Tel.: +43 1 58801-376526 Email address: galffy@acin.tuwien.ac.at (A. Galffy)
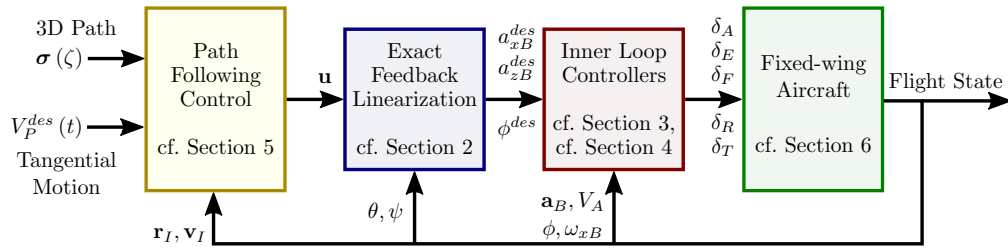
Figure 1: Overview of the proposed PFC concept of a fixed-wing aircraft.

is also investigated in Muniraj et al. (2017) for comparison reasons. In the latter work, a comparison of the root mean square (RMS) path error for a circular path with a radius of $100\,\mathrm{m}$ is shown to be $4.71\,\mathrm{m}$ for the nonlinear guidance logic, which can be reduced to $3.56\,\mathrm{m}$ by the LPV concept of Muniraj et al. (2017). A common approach for PFC of UAVs is to follow a virtual target, e.g., also applied in Cichella et al. (2011), similarly to the carrot-chasing algorithm, which was first introduced by Micaelli and Samson (1994) for two-steering-wheels mobile robots. In this context, Lugo-Cárdenas et al. (2017) introduces a Lyapunov based 3D PFC for fixed-wing UAVs comprising a virtual particle. In contrast to hierarchical designs, Mullen et al. (2016) introduces another integrated non-cascaded design based on filtered dynamic inversion for altitude control.

Most of the stated PFC concepts explicitly or implicitly assume that controlling the aircraft's attitude can drive the aircraft towards a desired position, for example, that the heading of the aircraft approximately correlates to the flight direction to justify a small angle approximation. For wind speeds in the order of the aircraft's airspeed, this assumption does not hold anymore, as significant attitude corrections like wind correction angles up to $90°$ would be required. In this context, controlling the vehicle acceleration instead of the vehicle attitude is promising to make explicit calculations of correction angles dispensable and to include feedforward path accelerations. In Ahsun et al. (2015), a height control is investigated without controlling the pitch angle. By controlling the vertical acceleration, the motion of the aircraft is restricted to a 2D-plane, which is comparable to the objectives of PFC. The LQR approach in Ratnoo et al. (2011) maps the cross-track error to a cross-track acceleration. This can be seen as a very specific case of the PFC concept of this work for constant altitude. To extend these 1D approaches to a more general 3D acceleration control, a nonlinear transformation is derived in Section 2 of this paper based on feedback linearization. For the special case of level turns, this 3D transformation corresponds to well-known sine and cosine relations of centripetal acceleration and vertical acceleration depending on the bank angle. Furthermore, acceleration control facilitates the inclusion of acceleration constraints, which appear to be a more direct approach to the limitations of a fixed-wing aircraft than the restriction of

course rates or yaw rates, as will be discussed in Section 6. In this context, system restrictions for PFC often are considered by introducing turn rate constraints, as it is the case in Yang et al. (2013), or by a minimum achievable path curvature in Gates (2010).

The use of direct lift control is discussed in early-stage research on flight control Pinsker (1970), as well as in more recent studies Merat (2008), Jaiswal et al. (2016), and Di Francesco et al. (2015). By using dynamic flap actuation, the lift, and therefore the vertical acceleration, can be manipulated more quickly than by rotating the whole aircraft by means of the elevator. The benefits of direct and consequently faster vertical acceleration response show to be beneficial for turbulence suppression, automatic landing performance and piloting qualities. To overcome performance limitations, in this paper the combined use of direct and indirect lift is proposed, where flap deflection is used as primary control input, and the elevator serves for maintaining the wings in their operational range and returning the flaps to their desired position.

The nonlinearities for PFC of a fixed-wing aircraft arise from combined effects of gravity, attitude, airspeed, nonlinear characteristics of forces and moments, and nonlinear path dynamics. Figure 1 gives an overview of the PFC concept with references to the corresponding sections and quantities. The gravitational acceleration and attitude effects are systematically addressed and can be included in the control concept by means of exact feedback linearization in Section 2. Nonlinear effects due to varying airspeed and thrust characteristics are taken into account at the design of the inner loop acceleration control in Section 3. In Section 4, further attention is given to the generation of vertical acceleration comprising effects of direct lift control. Based on the inner loop acceleration control, the dynamics of nonlinear paths are incorporated into the design of the path following control by means of path acceleration feedforward in Section 5. In Section 6, the UAV test platform is presented and the performed flight tests and results are demonstrated and discussed. Finally, conclusions and an outlook on future work are provided in Section 7.

2

2. Mathematical Modeling

In this section, a reduced model of a fixed-wing aircraft is derived, which significantly simplifies the subsequent design of the path following control. By exact feedback linearization a nonlinear transformation is found which converts desired accelerations of the path following controller into desired values for the inner loop acceleration control. Thereby, the nonlinear effects of gravity and aircraft orientation are thoroughly taken into account.

For modeling the fixed-wing aircraft dynamics, the aircraft is considered to be a rigid body. Two reference frames are used. Firstly, the inertial frame (Index I) is defined according to the North-East-Down coordinate system, which is also known as local tangent plane (LTP). It has a fixed origin on the surface of the earth with the x-axis to the North, y-axis to the East, and the z-axis according to a right-handed system pointing Down. Secondly, the body reference frame (Index B) is chosen to have its origin at the center of gravity of the aircraft with the x-axis in longitudinal direction, the y-axis in lateral direction pointing to the right wing, and the z-axis in vertical direction pointing down.

By representing the acting forces $\mathbf{f}_B$ and moments $\boldsymbol{\tau}_B$ in the body reference frame, the state-space model of a rigid body can be found as

$$\dot{\mathbf{r}}_I = \mathbf{R}_I^B\left(\varphi, \theta, \psi\right)\mathbf{v}_B \tag{1a}$$

$$\dot{\mathbf{v}}_B = \frac{1}{m}(\mathbf{f}_B - \boldsymbol{\omega}_B \times (m\mathbf{v}_B)) \tag{1b}$$

$$\dot{\boldsymbol{\theta}}_{RPY} = \mathbf{R}_{RPY}^B\left(\varphi, \theta\right)\boldsymbol{\omega}_B \tag{1c}$$

$$\dot{\boldsymbol{\omega}}_B = \mathbf{I}_B^{-1}(\boldsymbol{\tau}_B - \boldsymbol{\omega}_B \times (\mathbf{I}_B\boldsymbol{\omega}_B)) \ , \tag{1d}$$

where $\mathbf{r}_I = \begin{bmatrix} x_I & y_I & z_I \end{bmatrix}^{\mathrm{T}}$ is the position represented in the inertial reference frame, $\mathbf{v}_B$ the velocity represented in the body reference frame, $\boldsymbol{\theta}_{RPY} = \begin{bmatrix} \varphi & \theta & \psi \end{bmatrix}^{\mathrm{T}}$ the orientation expressed in Roll-Pitch-Yaw representation, $\boldsymbol{\omega}_B = \begin{bmatrix} \omega_{xB} & \omega_{yB} & \omega_{zB} \end{bmatrix}^{\mathrm{T}}$ the angular rates represented in the body reference frame, $\mathbf{R}_I^B$ the rotation matrix from the body frame to the inertial frame, $\mathbf{R}_{RPY}^B$ the transformation matrix from the body angular rates to Roll-Pitch-Yaw rates, $\mathbf{I}_B$ the moments of inertia represented in the body reference frame, and m the mass of the aircraft. A detailed derivation of the state-space model (1) can be found, e.g., in Stengel (2004) and L'Afflitto (2017). The expressions for the matrices $\mathbf{R}_I^B$ and $\mathbf{R}_{RPY}^B$ read as

$$\mathbf{R}_I^B = \begin{bmatrix} \cos(\psi) & -\sin(\psi) & 0 \\ \sin(\psi) & \cos(\psi) & 0 \\ 0 & 0 & 1 \end{bmatrix} \begin{bmatrix} \cos(\theta) & 0 & \sin(\theta) \\ 0 & 1 & 0 \\ -\sin(\theta) & 0 & \cos(\theta) \end{bmatrix}$$
$$\cdot \begin{bmatrix} 1 & 0 & 0 \\ 0 & \cos(\varphi) & -\sin(\varphi) \\ 0 & \sin(\varphi) & \cos(\varphi) \end{bmatrix} \tag{2}$$

and

$$\mathbf{R}_{RPY}^B = \begin{bmatrix} 1 & \sin(\varphi)\tan(\theta) & \cos(\varphi)\tan(\theta) \\ 0 & \cos(\varphi) & \sin(\varphi) \\ 0 & \sin(\varphi)\sec(\theta) & \cos(\varphi)\sec(\theta) \end{bmatrix} \ . \tag{3}$$

In general, the dynamics of a specific aircraft design result from the dependencies of the acting forces $\mathbf{f}_B$ and moments $\boldsymbol{\tau}_B$ on the 12 rigid body states $\mathbf{r}_I, \mathbf{v}_B, \boldsymbol{\theta}_{RPY}, \boldsymbol{\omega}_B$, and the physical inputs, namely the deflection of the aileron δ_A, the elevator δ_E, the flaps δ_F, the rudder δ_R, and the throttle input δ_T. The forces $\mathbf{f}_B$ basically consist of the lift L, the drag D, the thrust T, the side force SF, and the gravitational force, which need to be oriented correctly. An example of the corresponding mathematical expressions is the equation for modeling the lift force L, which will be referenced in Section 3,

$$L = c_L \frac{\rho}{2}V_A^2 S \tag{4a}$$

$$c_L \approx c_{L0} + c_{L,\alpha}\,\alpha + c_{L,\omega_{yB}}\,\omega_{yB} + c_{L,\delta_E}\,\delta_E + c_{L,\delta_F}\,\delta_F \ , \tag{4b}$$

where ρ denotes the air density, V_A the true airspeed, S the wing area, and c_L the lift coefficient. The latter is usually approximated using an affine representation of the angle of attack α, the angular rate ω_{yB}, and the deflections of the elevator δ_E and of the flaps δ_F.

2.1. Translational Model and Feedback Linearization

The following considerations aim at reducing the rigid body model (1) to the 6 states of translation, i.e., $\mathbf{r}_I$ and $\mathbf{v}_I$. Thereafter, for the reduced model a nonlinear transformation is found, which results in an exactly linear plant behavior $\frac{\mathrm{d}^2\mathbf{r}_I}{\mathrm{d}t^2} = \mathbf{u}$, with the new control input $\mathbf{u}$. To this end, the following assumptions are made:

- The accelerations a_{xB} and a_{zB}, as well as the roll angle φ are assumed to be controlled by ideal inner loop controllers. In practice, this means that the dynamics of the inner loops are sufficiently faster than the outer control loop.

- The flight state is coordinated, i.e., $a_{yB} = 0$. Hence, to obtain a lateral acceleration in the inertial frame a rotation by φ is required which results in a lateral component of a_{zB}.

- $\mathbf{a}_B$ complies with accelerations measured by accelerometers which are not capable of measuring the gravitational acceleration g, as gravity is a body force. Thus, the total acceleration acting on the aircraft is $\mathbf{a}_I = \mathbf{g} + \mathbf{R}_I^B\,\mathbf{a}_B$, with $\mathbf{g} = \begin{bmatrix} 0 & 0 & g \end{bmatrix}^{\mathrm{T}}$.

Under these assumptions, by splitting $\mathbf{R}_I^B$ into $\mathbf{D}(\theta, \psi)$ and a canonical rotation about the body x-axis by φ, the

3

kinematic model reads as

$$\frac{\mathrm{d}^2 \mathbf{r}_I}{\mathrm{d}t^2} = \begin{bmatrix} 0 \\ 0 \\ g \end{bmatrix} + \mathbf{D}(\theta,\psi) \begin{bmatrix} a_{xB} \\ a_{zB}\sin(\varphi) \\ a_{zB}\cos(\varphi) \end{bmatrix} \qquad (5a)$$

$$\mathbf{D}(\theta,\psi) = \begin{bmatrix} \cos(\theta)\cos(\psi) & \sin(\psi) & \sin(\theta)\cos(\psi) \\ \cos(\theta)\sin(\psi) & -\cos(\psi) & \sin(\theta)\sin(\psi) \\ -\sin(\theta) & 0 & \cos(\theta) \end{bmatrix} . \qquad (5b)$$

For $\mathbf{D}$ being a rotation matrix of yaw rotation ψ and thereafter pitch rotation θ, $\mathbf{D}$ is an element of SO(3). Therefore, $\mathbf{D}$ is orthogonal for arbitrary yaw and pitch angles.

Based on the assumption that a_{xB}, a_{zB}, and φ can be ideally controlled by inner loop controllers, the following nonlinear transformation

$$\begin{bmatrix} a_{xB} \\ a_{zB,S} \\ a_{zB,C} \end{bmatrix} = \begin{bmatrix} a_{xB} \\ a_{zB}\sin(\varphi) \\ a_{zB}\cos(\varphi) \end{bmatrix} = \mathbf{D}(\theta,\psi)^{-1} \left(\begin{bmatrix} 0 \\ 0 \\ -g \end{bmatrix} + \mathbf{u} \right) , \qquad (6)$$

with the new control input $\mathbf{u}$, yields an exact linear behavior of the plant and reduces (5) to

$$\frac{\mathrm{d}^2 \mathbf{r}_I}{\mathrm{d}t^2} = \mathbf{u} . \qquad (7)$$

The reference values a_{zB} and φ to be realized by the inner control loops can be calculated as

$$-a_{zB} = \sqrt{a_{zB,C}^2 + a_{zB,S}^2} \qquad (8a)$$

$$\varphi = \arctan\left(\frac{a_{zB,S}}{a_{zB,C}} \right) . \qquad (8b)$$

To maintain the analogy to the lift L, $-a_{zB}$ is used instead of a_{zB}. Note that $-a_{zB}$ is claimed to be positive, which means that desired accelerations below weightlessness are not considered in this paper. The roll angle φ is claimed to fulfill $|\varphi| < \frac{\pi}{2}$, which means that inverted flight is not considered either. As a consequence, the solution of (8) is unambiguous.

With (5) and the transformations (6) and (8), a representation of a fixed-wing aircraft is found, which is perfectly suitable for a path following control of the output $\mathbf{r}_I$ by means of the inner loop controllers for a_{xB}, a_{zB}, and φ. The resulting system (7) appears in Brunovsky form with vector relative degree $\{2,2,2\}$ for the output $\mathbf{r}_I = \begin{bmatrix} x_I & y_I & z_I \end{bmatrix}^T$, see, e.g., Isidori (2013), which significantly simplifies the design of the path following controller. Considering the full dynamics of the rigid body model (1), the 3 rotational degrees of freedom, i.e., $\boldsymbol{\theta}_{RPY}$, are neglected. Addressing these 6 remaining states as zero dynamics of the system, the question may be raised, whether these dynamics are stable. As the roll angle φ constitutes an output of the inner loop control, its stability is given by the stability of the corresponding controller. For the case

on hand that the translational motion is specified, the stability of the pitch angle θ and yaw angle ψ relate to the stability of the angle of attack α and sideslip angle β, i.e., the longitudinal and directional stability of the aircraft. The specific values of θ and ψ are not calculated explicitly, but result from the desired translational motion and the current wind situation, as part of the stable zero dynamics. Therefore, explicit calculations of wind correction angles become dispensable.

3. Inner Loop Controllers

The nonlinear transformation (6) to obtain the exactly linearized system (7) relies on the assumption that φ, a_{xB}, and a_{zB} are realized by the inner loop controllers with sufficient accuracy. To obtain high bandwidth reference tracking and disturbance rejection, the inner loop control is designed to track directly measurable quantities like angular rates and accelerations. In the context of flight control, turbulence may cause severe disturbances to these kinematic quantities. Furthermore, aerodynamic forces show a nonlinear dependence on the airspeed and orientation of the aircraft. However, expressed in the body frame and corrected for nonlinear effects of the varying airspeed V_A, the dynamics turn out to be sufficiently linear to allow for a linear controller design.

Figure 2 shows a scheme of the inner loop control, which transforms desired values φ^{des}, δ_F^{des}, a_{zB}^{des}, a_{yB}^{des}, and a_{xB}^{des} from the outer loop to the control inputs δ_A, δ_E, δ_F, δ_R, and δ_T of the aircraft. In principle, individual SISO controllers are designed under the assumption that the effects of the inputs are sufficiently decoupled[1]. For the implementation of "Direct Lift Control", a combined control of δ_E and δ_F is proposed, which will be explained in more detail in Section 4. With direct lift control another degree of freedom emerges, which is utilized to introduce a desired flap deflection δ_F^{des}, as indicated in Figure 2.

The identification task is accomplished during test flights where a chirp signal is applied to the respective input. To reduce the influence of external disturbances, the identification maneuver can be executed multiple times. As an example, Figure 3 shows the measured mean response of the roll rate ω_{xB} to a chirp signal of the aileron δ_A, where the signals of four identification maneuvers were averaged. Based on the mean response the discrete-time SISO transfer function $P_{\delta_A,\omega_{xB}}^z(z)$ from δ_A to ω_{xB} can be determined using a classical least squares approach, see, e.g., Ljung (1998). The identified plants used for the controller design are listed in Table 1 with the corresponding sampling time $T_s = 0.02\,\mathrm{s}$. In total, five identification maneuvers were performed, i.e., one for each control input. Thus, a pretty low identification effort is necessary,

---

[1]Coupling effects like adverse yaw and parasitic moments due to the propeller slipstream are not included. MIMO structures may be utilized to include such coupling effects, however, this increases the complexity for identification and implementation.
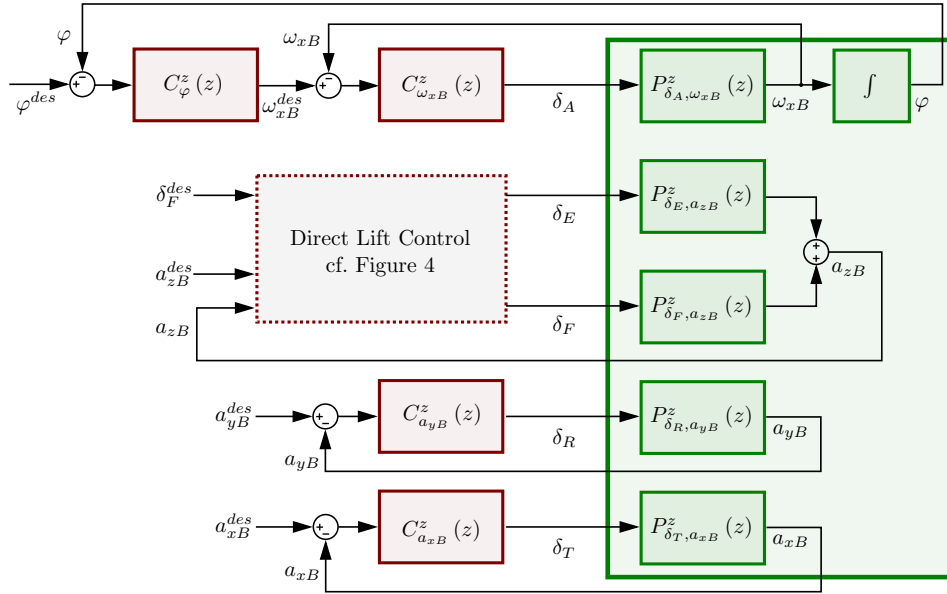
4

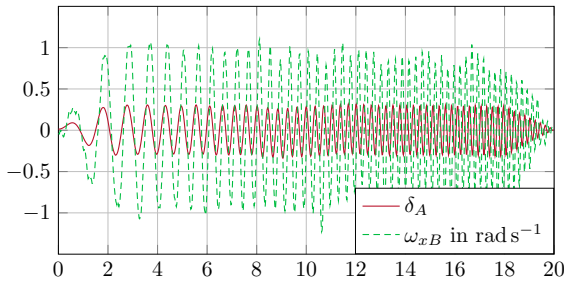Figure 2: Cascade of SISO output controllers.

Figure 3: Mean response of ω_{xB} to the chirp signal of δ_A.

which is limited to SISO transfer functions from the control inputs to the corresponding kinematic quantities, i. e., $P^z_{\delta_A,\omega_{xB}}(z)$ from δ_A to ω_{xB}, $P^z_{\delta_E,c_{zB}}(z)$ from δ_E to c_{zB}, $P^z_{\delta_F,c_{zB}}(z)$ from δ_F to c_{zB}, $P^z_{\delta_R,a_{yB}}(z)$ from δ_R to a_{yB}, and $P^z_{\delta_T,a_{xB}}(z)$ from δ_T to a_{xB}, where c_{zB} is the normalized coefficient of the vertical acceleration a_{zB}, which will be discussed in more detail in Section 4. As indicated in Figure 2, the control of φ is based on a cascaded structure with the intermediate control input ω_{xB}^{des}. Therefore, another transfer function $P^z_{\omega_{xB}^{des},\varphi}(z)$ from ω_{xB}^{des} to φ is required to design $C^z_\varphi(z)$. Assuming that $C^z_{\omega_{xB}}(z)$ matches the designed closed-loop behavior and with the relation $\omega_{xB} = \frac{d\varphi}{dt}$, the transfer function $P^z_{\omega_{xB}^{des},\varphi}(z)$ can be calculated without further test flights. During the identification maneuvers due care is taken to avoid exogenous disturbances. To this end, smooth weather conditions are cho-

sen for the identification test flights. Furthermore, kinematic quantities not being subject to the current identification maneuver are kept constant by feedback control, e. g., $\varphi^{des} = 0$ for the identification of the longitudinal dynamics. In this context, also a pitch controller cascade or an airspeed controller cascade may be designed analogously to the roll controller $C^z_\varphi(z)$, $C^z_{\omega_{xB}}(z)$ cascade to keep $\theta^{des} = $ const. or $V_A^{des} = $ const. for the identification flights of the lateral dynamics.

The PI-controllers $C^z_{\omega_{xB}}(z)$, $C^z_{a_{yB}}(z)$, $C^z_{a_{xB}}(z)$, cf. Figure 2, are designed with the classical loop-shaping method in the frequency domain by utilizing the tustin transformation, see, e. g., Franklin et al. (1998). Still, the nonlinear dependencies on the airspeed V_A have to be taken into account. The magnitude of the transfer function from δ_A to ω_{xB} is directly proportional to the airspeed V_A. By applying a multiplicative correction factor $\frac{V_{ref}}{V_A}$, where V_{ref} is the reference airspeed for which the controller is designed, this known relation is compensated. With the output error $e_{\omega_{xB}} = \omega_{xB}^{des} - \omega_{xB}$, the corresponding integral error $e_{I,\omega_{xB}}$, and the notation $\delta_A^k = \delta_A(kT_s)$, $V_A^k = V_A(kT_s)$, $e^k_{\omega_{xB}} = e_{\omega_{xB}}(kT_s)$, and $e^k_{I,\omega_{xB}} = e_{I,\omega_{xB}}(kT_s)$, for the k-th sampling point, the PI control law reads as

$$\delta_A^k = \frac{V_{ref}}{V_A^k}\left(k_P e^k_{\omega_{xB}} + k_I e^k_{I,\omega_{xB}}\right), \qquad (9)$$

where k_P and k_I denote the proportional and integral controller gains. The integral error $e^k_{I,\omega_{xB}}$ is calculated by the forward Euler method, i. e., $e^k_{I,\omega_{xB}} = e^{k-1}_{I,\omega_{xB}} + T_s e^k_{\omega_{xB}}$ with the sampling time $T_s = 0.02$ s.

In a similar way, the nonlinear dependence on the airspeed is taken into account for the other transfer functions, see Table 1. For instance, the magnitude of the transfer function from δ_R to a_{yB} shows a quadratic dependence on the airspeed V_A, as a_{yB} is generated by sideforce, which can be modeled according to (4). Thus, the effect of V_A due to the dynamic pressure, i.e., $\frac{\rho}{2}V_A^2$, is compensated by a quadratic correction factor $\frac{V_{ref}^2}{V_A^2}$ in an analogous manner to (9). Similarly, the proportional influence of the air density ρ may also be compensated.

As the value of a_{xB} depends on the generated thrust T, the transfer function from δ_T to a_{xB} comprises nonlinearities of the motor and propeller characteristics. One simple possibility to include these nonlinearities in the control design is to determine a static mapping $T(\delta_T, V_A)$, i.e. the steady-state thrust T as a function of δ_T and V_A. To this end, test bench measurements or CFD simulations can be performed. Subsequently, for known V_A, the mapping $T(\delta_T, V_A)$ can be used to compensate for this static nonlinearity. Still, the performance of a conventional PI-controller $C_{a_{xB}}^z(z)$ without any correction proved to be sufficient for the objective to validate the PFC concept.

The controllers are designed such that an open-loop phase reserve of about $\Phi_{0dB} = 60°$ results, where the crossover frequency Ω_{0dB} is specified in the Tustin domain. The resulting controller gains k_P and k_I are summarized in Table 2 together with the corresponding crossover frequencies Ω_{0dB} and phase reserves Φ_{0dB}. The controllers $C_{a_{zB}}^z(z)$ and $C_{\delta_F}^z(z)$ are part of the direct lift control and are explained in the next section.

4. Direct Lift Control

Direct lift control can be used to improve the dynamic response of lift generation and to control the lift independently from the orientation. By using dynamic flap actuation, the lift, and therefore the vertical acceleration, can be manipulated more quickly than by rotating the whole aircraft by means of the elevator. Thus, in the proposed concept, flap deflection is used as primary control input, and the elevator serves for maintaining the wings in their operational range and returning the flaps to their desired position. Furthermore, an angle of attack oscillation is found to cause an antiresonance, which lowers the effectiveness of direct lift control. Hence, the dynamic response of lift generation is further improved by using a feedforward filter, which anticipates and reduces this oscillation effect. For the particular aircraft under investigation, the novel concept allows to more than double the bandwidth of the vertical acceleration controller compared to classical approaches.[2]

In this regard, Figure 4 shows the control structure to realize a desired vertical acceleration a_{zB}^{des} with a desired

---
[2]Patent pending.

flap angle δ_F^{des} by combining the control inputs δ_E and δ_F. $C_{a_{zB}}^z(z)$ is the primary controller, which tracks the desired vertical acceleration a_{zB}^{des} by means of flap deflection δ_F. $C_{\delta_F}^z(z)$ acts in the sense of a dual stage control and returns low frequency flap deflection δ_F to a desired value δ_F^{des} by means of the feedback elevator input $\delta_{E,FB}$. $F_{\delta_F,\delta_E}^z(z)$ is the mentioned feedforward filter which is designed to compensate for the antiresonance by means of a feedforward elevator input $\delta_{E,FF}$. Thus, the elevator deflection consists of the sum of $\delta_{E,FB}$ from $C_{\delta_F}^z(z)$ and $\delta_{E,FF}$ from $F_{\delta_F,\delta_E}^z(z)$.
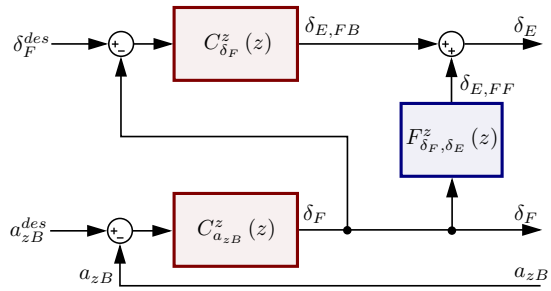

Figure 4: Structure of the direct lift control including $C_{a_{zB}}^z(z)$, $C_{\delta_F}^z(z)$ and the designed filter $F_{\delta_F,\delta_E}^z(z)$.

In the following, the phenomenon which causes the antiresonance, the design of the filter $F_{\delta_F,\delta_E}^z(z)$, and the design of the dual stage control $C_{a_{zB}}^z(z)$ and $C_{\delta_F}^z(z)$ will be briefly outlined. As a_{zB} mainly results from the acting lift force L and therefore depends on the dynamic pressure $\frac{\rho}{2}V_A^2$ in (4), instead of examining a_{zB} itself the normalized coefficient of vertical acceleration

$$c_{zB} = \frac{a_{zB}}{V_A^2} \frac{V_{ref}^2}{a_{ref}} \qquad (10)$$

is introduced, i.e., the quadratic dependence on the airspeed V_A is compensated. For choosing $a_{ref} = g = 9.81\,\mathrm{m\,s^{-2}}$, at level flight conditions with $V_A = V_{ref}$ follows $-c_{zB} = 1$. Due to the close relation of the acceleration a_{zB} and the force L, the coefficient c_{zB} is modeled similarly to c_L in (4) as

$$c_{zB} \approx c_{zB,0} + c_{zB,\alpha}\,\alpha + c_{zB,\delta_E}\,\delta_E + c_{zB,\delta_F}\,\delta_F\,. \qquad (11)$$

The generation of lift by elevator deflection δ_E is mainly based on changing the angle of attack α, i.e., the effect of $c_{zB,\alpha}\,\alpha$ in (11) dominates. This indirect lift generation shows second order low-pass characteristics, as the change of α corresponds to a rotation of the aircraft according to the so called short-period mode. The additional direct component $c_{zB,\delta_E}\,\delta_E$ is a parasitic effect of the elevator due to the force at the horizontal tail, which is necessary to generate the pitching moment to change the angle of attack. In the case of a tailplane, this parasitic force results to be opposite to the resulting lift of the wing, i.e., a non-minimum phase characteristics can be observed. Therefore, generation of lift by the elevator inevitably entails

6

Input	Output	Transfer function	Nonlinearity
δ_A	ω_{xB}	$P^z_{\delta_A,\omega_{xB}}(z) = \dfrac{-0.24z^{-1}+0.75z^{-2}-0.17z^{-3}}{1-1.85z^{-1}+1.25z^{-2}-0.30z^{-3}}$	V_A
δ_E	a_{zB}	$P^z_{\delta_E,c_{zB}}(z) = \dfrac{-0.14+0.085z^{-1}+0.22z^{-2}}{1-1.57z^{-1}+0.63z^{-2}}$	V_A^2
δ_F	a_{zB}	$P^z_{\delta_F,c_{zB}}(z) = \dfrac{1.21-2.12z^{-1}+0.98z^{-2}}{1-1.48z^{-1}+0.53z^{-2}}$	V_A^2
δ_R	a_{yB}	$P^z_{\delta_R,a_{yB}}(z) = \dfrac{-0.43z^{-1}-1.12z^{-2}+1.83z^{-3}}{1-1.21z^{-1}-0.035z^{-2}+0.28z^{-3}}$	V_A^2
δ_T	a_{xB}	$P^z_{\delta_T,a_{xB}}(z) = \dfrac{0.054z^{-1}+0.44z^{-2}-0.85z^{-3}+0.76z^{-4}}{1-1.23z^{-1}+0.41z^{-2}-0.16z^{-3}+0.044z^{-4}}$	$T(\delta_T,V_A)$

Table 1: Identified transfer functions of the five control inputs by test flights and nonlinear dependencies on the air speed V_A.

Controller	k_P	k_I	$\Omega_{0\text{dB}}$	$\Phi_{0\text{dB}}$
$C^z_{\omega_{xB}}(z)$	0.1278	2.9485	$10\,\text{rad s}^{-1}$	$55.73°$
$C^z_{a_{zB}}(z)$	0.4773	10.1479	$15\,\text{rad s}^{-1}$	$58.31°$
$C^z_{a_{yB}}(z)$	0.0415	0.2347	$2\,\text{rad s}^{-1}$	$56.41°$
$C^z_{a_{xB}}(z)$	0.1817	0.8651	$10\,\text{rad s}^{-1}$	$69.32°$
$C^z_{\delta_F}(z)$	-0.1948	-1.1025	$3\,\text{rad s}^{-1}$	$60.91°$
$C^z_{\varphi}(z)$	2.9442	1.7560	$3\,\text{rad s}^{-1}$	$60.60°$

Table 2: Control gains k_P and k_I, crossover frequency $\Omega_{0\text{dB}}$, and open-loop phase reserve $\Phi_{0\text{dB}}$ of the PI controllers.

a lag due to the low-pass characteristics, which depends on the short-period mode, and in case of a tailplane the polarity of the force at first even results to be opposite to the desired one.

In contrast, for direct lift control the generation of lift by flap deflection δ_F directly influences the component $c_{zB,\delta_F}\,\delta_F$ of (11) as primary effect. If no parasitic pitching moment is caused by the wing deformation, the stationary value of the angle of attack α remains the same, i.e., $c_{zB,\alpha}\,\alpha$ does not change for very low excitation frequencies. Still a dynamic effect is observed, which causes an oscillation of α. This oscillation brings along an antiresonance approximately at the resonance frequency of the short-period mode, where the phase has got a shift of 90°. This phase shifted oscillation results in a secondary effect $c_{zB,\alpha}\,\alpha$ in (11), which cancels out part of the desired component $c_{zB,\delta_F}\,\delta_F$. The mentioned oscillation of α is caused by the vertical motion of the aircraft which sets in for dynamic lift variation by δ_F. Namely, if δ_F by means of $c_{zB,\delta_F}\,\delta_F$ excites a sinusoidal acceleration, a sinusoidal flight trajectory will set in, where maximum upwards acceleration is found at minimum height. For low excitation frequencies, the pitch angle follows the change of orientation of the trajectory due to the characteristics of the aircraft to orient into the airflow, i.e., to keep α constant. For higher excitation frequencies, the aircraft orientation does not follow the trajectory direction ideally anymore due to the low pass-characteristics of the short-period mode. As the short-period mode decouples for higher frequencies,

the pitch angle oscillates with a phase lag. In the frequency range of the short-period mode resonance, this phase lag is such that a negative angle of attack α occurs for positive flap deflection. Therefore, a negative effect $c_{zB,\alpha}\,\alpha$ cancels out part of the intended positive effect $c_{zB,\delta_F}\,\delta_F$. Thus, the outlined phenomenon causes an antiresonance, which lowers the effectiveness of direct lift control in the frequency range of the short-period mode resonance.

To improve the effectiveness of direct lift control, a dynamic filter $F^z_{\delta_F,\delta_E}(z)$ is designed to compensate the described antiresonance by use of δ_E. To this end, the input δ_F is filtered and the output of the dynamic filter is added to δ_E, as indicated in Figure 4. The intention is to reduce the oscillation of α by anticipating the effect of δ_F and compensating it with δ_E, i.e., adding a feedforward elevator deflection $\delta^z_{E,FF} = F^z_{\delta_F,\delta_E}(z)\,\delta^z_F$ to the control input δ_E. To this end, the transfer functions $P^z_{\delta_E,c_{zB}}(z)$ with $\delta_F = 0$, and $P^z_{\delta_F,c_{zB}}(z)$ with $\delta_E = \delta_{E,0} = \text{const.}$ are identified, cf. Table 1. For the design of the filter $F^z_{\delta_F,\delta_E}(z)$ the transfer functions are transformed into the Tustin domain by applying the bilinear transformation $z = \frac{1+q\,T_s/2}{1-q\,T_s/2}$, resulting in $P^q_{\delta_E,c_{zB}}(q)$ and $P^q_{\delta_F,c_{zB}}(q)$. Please note that the sampling rate is much higher than the considered system dynamics. Thus, the Tustin variable q also approximates the continuous Laplace variable s in the regime of the short-period mode. Assuming linear superposition, the new resulting transfer function $\tilde{P}^q_{\delta_F,c_{zB}}(q)$ from δ_F to $-c_{zB}$ with $\delta^q_{E,FF} = F^q_{\delta_F,\delta_E}(q)\,\delta^q_F$ becomes

$$-c^q_{zB} = P^q_{\delta_F,c_{zB}}\delta^q_F + P^q_{\delta_E,c_{zB}}\delta^q_{E,FF} =$$
$$= \underbrace{\left(P^q_{\delta_F,c_{zB}} + F^q_{\delta_F,\delta_E}P^q_{\delta_E,c_{zB}}\right)}_{\tilde{P}^q_{\delta_F,c_{zB}}}\delta^q_F \ . \qquad (12)$$

To compensate for the phase lag, a lead filter of second order is chosen in the Tustin domain in the form

$$F^q_{\delta_F,\delta_E}(q) = \frac{b_1 q + b_2 q^2}{q^2 + 2\xi_F\omega_F q + \omega_F^2} \ . \qquad (13)$$

An optimization problem is solved to find an optimal fit of $\tilde{P}^q_{\delta_F,c_{zB}}(q)$ to a desired plant $\tilde{P}^{q,des}_{\delta_F,c_{zB}}(q)$. The cost function to be minimized with respect to the parameters b_1, b_2, ξ_F,

7

and ω_F is chosen as

$$J = \sum_{\Omega_k \in \Omega} \left| \left| \tilde{P}^q_{\delta_F,c_{z_B}}(j\,\Omega_k) \right| - \left| \tilde{P}^{q,des}_{\delta_F,c_{z_B}}(j\,\Omega_k) \right| \right| , \quad (14)$$

with $\Omega = 2\pi\{0.3; 0.4; \ldots; 3.9; 4\}$. Thus, the magnitude response is optimized at 38 equally spaced frequencies in proximity to the short-period resonance frequency $\omega_{SP} = 2\pi f_{SP} = 13.15\,\mathrm{rad\,s}^{-1}$. The phase response is not included in the cost function, as the time delay of the system was not determined explicitly and cannot be compensated by a causal filter. For the desired plant $\tilde{P}^{q,des}_{\delta_F,c_{z_B}} = \lim_{\Omega\to\infty}\left| P^q_{\delta_F,c_{z_B}}(j\Omega)\right| = 1.45$, the optimized filter parameters result in $b_1 = 18.15$, $b_2 = 0.968$, $\xi_F = 0.991$, and $\omega_F = 20.04\,\mathrm{rad\,s}^{-1}$. Figure 5 depicts the Bode plots of the original plant $P^q_{\delta_F,c_{z_B}}(q)$, the desired plant $\tilde{P}^{q,des}_{\delta_F,c_{z_B}}(q)$, the filter $F^q_{\delta_F,\delta_E}(q)$, and the resulting plant $\tilde{P}^q_{\delta_F,c_{z_B}}(q)$.
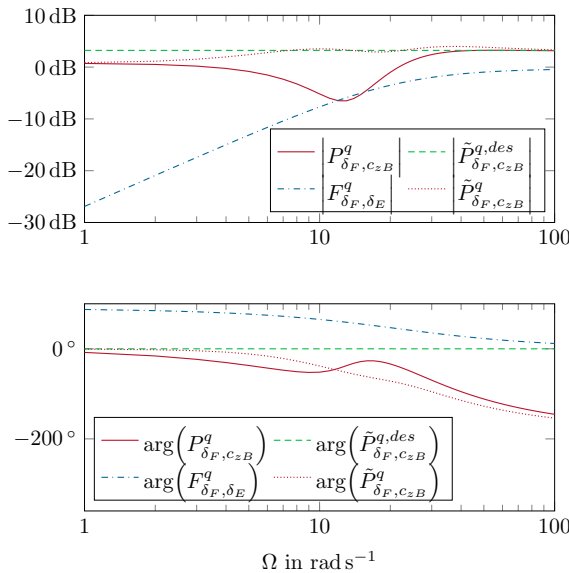

Figure 5: Bode plots of original plant $P^q_{\delta_F,c_{z_B}}(j\Omega)$, desired plant $\tilde{P}^{q,des}_{\delta_F,c_{z_B}}(j\Omega)$, filter $F^q_{\delta_F,\delta_E}(j\Omega)$, and resulting plant $\tilde{P}^q_{\delta_F,c_{z_B}}(j\Omega)$.

For implementation, the filter (13) designed in the Tustin domain is transformed to the z-domain by applying the inverse bilinear transformation $q = \frac{2}{T_s}\frac{z-1}{z+1}$, with $T_s = 0.02\,\mathrm{s}$, resulting in

$$F^z_{\delta_F,\delta_E}(z) = \frac{0.7997 - 1.347z^{-1} + 0.5472z^{-2}}{1 - 1.336z^{-1} + 0.4474z^{-2}} . \quad (15)$$

Figure 6 illustrates the effect of the filter by comparing the time evolution of $-c_{z_B}$ in response to a chirp signal in δ_F without and with the filter $F^z_{\delta_F,\delta_E}(z)$, which were measured during identification test flights. In the time interval from $2\,\mathrm{s}$ to $12\,\mathrm{s}$, frequencies in the range of $2\,\mathrm{Hz}$ are
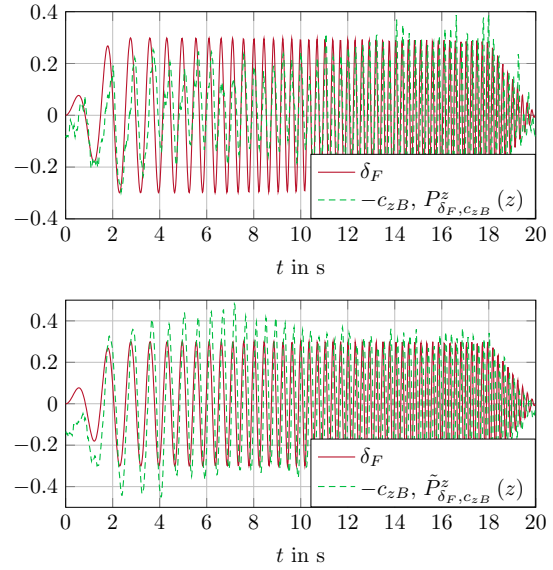

Figure 6: Measured response $-c_{z_B}$ to the chirp of δ_F without $F^z_{\delta_F,\delta_E}(z)$ (top) and with $F^z_{\delta_F,\delta_E}(z)$ resulting in $\tilde{P}^z_{\delta_F,c_{z_B}}(z)$ (bottom).

excited. This corresponds to the frequency band where the antiresonance occurs. The antiresonance is clearly evident in the response without the filter $F^z_{\delta_F,\delta_E}(z)$, which is illustrated in the upper plot of Figure 6. The lower plot shows the time evolution of $-c_{z_B}$ including the filter $F^z_{\delta_F,\delta_E}(z)$, where the antiresonance is confirmed to be compensated. The resulting plant $\tilde{P}^z_{\delta_F,c_{z_B}}(z)$, cf. (12), is identified to be

$$\tilde{P}^z_{\delta_F,c_{z_B}}(z) = \frac{0.137 + 0.135z^{-1}}{1 - 1.25z^{-1} + 0.44z^{-2}} . \quad (16)$$

For this plant, a PI controller $C^z_{c_{z_B}}(z)$, which tracks

$$c^{des}_{z_B} = \frac{a^{des}_{z_B}}{V^2_A}\frac{V^2_{ref}}{a_{ref}} \quad (17)$$

is designed with the classical loop-shaping method in the frequency domain by utilizing the Tustin transformation. With a notation analogous to (9), the control law of $C^z_{c_{z_B}}(z)$ reads as

$$\delta^k_F = k_P e^k_{c_{z_B}} + k_I e^k_{I,c_{z_B}} . \quad (18)$$

By including the compensation of the nonlinear dependence on the current airspeed V^k_A, see (10) and (17), the corresponding control law of $C^z_{a_{z_B}}(z)$, cf. Figure 4, follows as

$$\delta^k_F = \frac{V^2_{ref}}{\left(V^k_A\right)^2 a_{ref}}\left(k_P e^k_{a_{z_B}} + k_I e^k_{I,a_{z_B}}\right) . \quad (19)$$

8

The controller parameters are listed in Table 2 together with the corresponding crossover frequency $\Omega_{0\text{dB}}$ and open-loop phase reserve $\Phi_{0\text{dB}}$.

The effective range of accelerations that can be generated by δ_F is limited. Furthermore, flaps parasitically generate drag for high deflections. Thus, a method is implemented to return δ_F to $\delta_F^{des} = 0$ by the elevator deflection $\delta_{E,FB}$ according to a dual stage control principle, cf. Figure 4. For active $C_{c_{zB}}^z(z)$ control with the corresponding plant $\tilde{P}_{\delta_F,c_{zB}}^z(z)$, the effect of δ_E on δ_F can be determined to be,

$$\delta_F^z = \underbrace{\frac{C_{c_{zB}}^z(z)}{1 - C_{c_{zB}}^z(z)\,\tilde{P}_{\delta_F,c_{zB}}^z(z)} P_{\delta_E,c_{zB}}^z(z)\,\delta_E^z}_{P_{\delta_E,\delta_F}^z(z)} , \qquad (20)$$

as $c_{zB,\delta_E}^z = P_{\delta_E,c_{zB}}^z(z)\,\delta_E^z$ acts as output disturbance, which propagates to the control input δ_F according to the closed-loop transfer function $\frac{C_{c_{zB}}^z(z)}{1 - C_{c_{zB}}^z(z)\tilde{P}_{\delta_F,c_{zB}}^z(z)}$. For $P_{\delta_E,\delta_F}^z(z)$, the PI controller $C_{\delta_F}^z(z)$ is designed with considerably lower bandwidth compared to $C_{c_{zB}}^z(z)$ to prevent interactions of the two controllers as can be seen in Table 2. In the case that a steady flap deflection is required for slow flight, e.g., for take-off and landing, δ_F^{des} can also be specified to $\delta_F^{des} > 0$. However, the input limits of δ_F must be considered to maintain enough control input range for $C_{c_{zB}}^z(z)$.

Finally, the functionality of the direct lift control concept is illustrated in Figure 7. The lift curve $-c_{zB}(\alpha)$ shows a typical dependence of c_{zB} on the angle of attack α. The effect of the flaps δ_F is to shift the curve $-c_{zB}(\alpha)$, upwards for positive δ_F. The effect of the elevator δ_E is to manipulate α to reach different points of $c_{zB}(\alpha)$, which constitutes the conventional method for varying the lift. The introduced control concept includes the flaps for highly dynamic c_{zB} variations. Figure 7 outlines the setpoint change from $-c_{zB,0}$ to $-c_{zB,1}$. First, the controller $C_{c_{zB}}^z(z)$ via the control input δ_F increases $-c_{zB}$ in a highly dynamic manner with a designed bandwidth of about $15\,\text{rad}\,\text{s}^{-1}$. Then the controller C_{δ_F} returns δ_F to the initial value, in this case $\delta_F^{des} = 0$, via the control input δ_E. The different dynamics are emphasized by the small arrows, which shall indicate constant time steps. Thus, the new value $c_{zB,1}$ is reached with the high dynamics of $C_{c_{zB}}^z(z)$, whereas the horizontal movement approximately on the level of $c_{zB,1}$ is based on a fifth of the bandwidth, thus, $3\,\text{rad}\,\text{s}^{-1}$.

The curve $-c_{zB}(\alpha)$ is pretty linear until the region around α_{max} where the wings begin to stall and lift decreases again. By setting a limitation to a value below $-c_{zB,max}$, e.g., $-c_{zB,1}$, a simple, but effective stall prevention can be implemented.

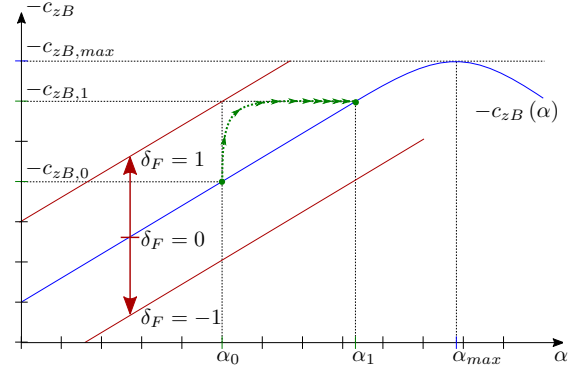Figure 7: Setpoint change from $-c_{zB,0}$ to $-c_{zB,1}$.

5. Path Following Control

Based on the system $\frac{\mathrm{d}^2}{\mathrm{d}t^2}\mathbf{r}_I = \mathbf{u}$, cf. (7), the path following control for a fixed-wing aircraft is designed. The so-called path parameter ζ defines the desired path $\boldsymbol{\sigma}(\zeta)$ in parameterized form. Here, $\boldsymbol{\sigma}(\zeta)$ is required to be two times differentiable, and, if the resulting accelerations shall be continuous, two times continuously differentiable[3]. The derivatives are abbreviated as $\boldsymbol{\sigma}' = \frac{\partial\boldsymbol{\sigma}}{\partial\zeta}$ and $\dot{\zeta} = \frac{\mathrm{d}\zeta}{\mathrm{d}t}$.

The control objectives of PFC are defined as follows, Nielsen et al. (2010), Bischof et al. (2017):

- The output $\mathbf{r}_I$ converges asymptotically to the path $\boldsymbol{\sigma}(\cdot)$, i.e., $\inf_{\zeta}\|\mathbf{r}_I(t) - \boldsymbol{\sigma}(\zeta)\| \to 0$ for $t \to \infty$. (*asymptotic convergence*)

- If at t_0 the aircraft position $\mathbf{r}_I$ is on the path and the velocity $\mathbf{v}_I$ is parallel to the path, i.e., $\exists\zeta_0 : \mathbf{r}_I = \boldsymbol{\sigma}(\zeta_0) \wedge \mathbf{v}_I = \kappa\boldsymbol{\sigma}'(\zeta_0), \kappa \in \mathbb{R}$, then $\inf_{\zeta}\|\mathbf{r}_I(t) - \boldsymbol{\sigma}(\zeta)\| = 0$ for all $t \geq t_0$. (*invariance property*)

- The requirements for $\zeta(t)$ depend on the operation mode. (*tangential motion*)

Various operation modes which define the motion along the path can be considered. In the following, the path following control for a desired path speed is deduced. Considering the path error $\mathbf{e}_P = \mathbf{r}_I - \boldsymbol{\sigma}(\zeta)$, the error dynamics take the form

$$\mathbf{e}_P = \mathbf{r}_I - \underbrace{\boldsymbol{\sigma}(\zeta)}_{\mathbf{r}_P} \qquad (21\text{a})$$

$$\frac{\mathrm{d}}{\mathrm{d}t}\mathbf{e}_P = \mathbf{v}_I - \underbrace{\boldsymbol{\sigma}'(\zeta)\,\dot{\zeta}}_{\mathbf{v}_P} \qquad (21\text{b})$$

$$\frac{\mathrm{d}^2}{\mathrm{d}t^2}\mathbf{e}_P = \mathbf{u} - \underbrace{(\boldsymbol{\sigma}''(\zeta)\,\dot{\zeta}^2 + \boldsymbol{\sigma}'(\zeta)\,\ddot{\zeta})}_{\mathbf{a}_P} . \qquad (21\text{c})$$

---

[3]Henceforth, the dependence on the time $\mathbf{r}_I(t)$, $\zeta(t)$, etc. is omitted for clarity, except for special emphasis.

9

For the special case on hand, also analogies to a PID-control can be made. Therefore, the coefficients of the feedback terms are named k_P, k_I, and k_D. For

$$\mathbf{u} = \boldsymbol{\sigma}''(\zeta)\,\dot{\zeta}^2 + \boldsymbol{\sigma}'(\zeta)\,\ddot{\zeta} - k_P\,\mathbf{e}_P - k_D\,\frac{\mathrm{d}}{\mathrm{d}t}\mathbf{e}_P \ , \quad (22)$$

the desired error dynamics

$$\frac{\mathrm{d}^2}{\mathrm{d}t^2}\mathbf{e}_P + k_D\,\frac{\mathrm{d}}{\mathrm{d}t}\mathbf{e}_P + k_P\,\mathbf{e}_P = \mathbf{0} \quad (23)$$

can be specified by tuning the parameters $k_P > 0$ and $k_D > 0$ according to the characteristic polynomial $p(s) = s^2 + k_D s + k_P$, with the Laplace variable s. It is also possible to obtain individual dynamics for the different Cartesian axes by using the matrix $\mathbf{K}_P = \mathrm{diag}\left(\begin{bmatrix} k_{P1} & k_{P2} & k_{P3} \end{bmatrix}\right)$ instead of the scalar k_P, and $\mathbf{K}_D$ in an analogous manner. Furthermore, individual dynamics for other than the Cartesian axes of the inertial frame could be defined by use of nondiagonal $\mathbf{K}_P$ and $\mathbf{K}_D$. Henceforth, the case of scalar parameters is considered.

It seems reasonable to compare the designed error dynamics (23) to a three dimensional spring-damper-system, where the equilibrium point continuously changes according to the path parameter $\zeta(t)$ and the corresponding path position $\boldsymbol{\sigma}(\zeta(t))$. Thus, the terms in (22) can be interpreted as spring action $-k_P\,\mathbf{e}_P$, damper action $-k_D\,\frac{\mathrm{d}}{\mathrm{d}t}\mathbf{e}_P$, acceleration feedforward $\boldsymbol{\sigma}''(\zeta)\,\dot{\zeta}^2$ due to the path parameter speed $\dot{\zeta}$, and acceleration feedforward $\boldsymbol{\sigma}'(\zeta)\,\ddot{\zeta}$ due to the path parameter acceleration $\ddot{\zeta}$.

By introducing an integral error $\frac{\mathrm{d}}{\mathrm{d}t}\mathbf{e}_I = \mathbf{e}_P$, the final control law for the input results in

$$\mathbf{u} = \boldsymbol{\sigma}''(\zeta)\,\dot{\zeta}^2 + \boldsymbol{\sigma}'(\zeta)\,\ddot{\zeta} - k_P\mathbf{e}_P - k_D\,\frac{\mathrm{d}}{\mathrm{d}t}\mathbf{e}_P - k_I\mathbf{e}_I \ . \quad (24)$$

Therefore, the error dynamics extend to

$$\frac{\mathrm{d}^3}{\mathrm{d}t^3}\mathbf{e}_P + k_D\,\frac{\mathrm{d}^2}{\mathrm{d}t^2}\mathbf{e}_P + k_P\,\frac{\mathrm{d}}{\mathrm{d}t}\mathbf{e}_P + k_I\,\mathbf{e}_P = \mathbf{0} \ , \quad (25)$$

with the additional tuning parameter $k_I > 0$ yielding the corresponding characteristic polynomial $p(s) = s^3 + k_D s^2 + k_P s + k_I$.

For the calculation of the control law (24), the time evolution of the path parameter $\zeta(t)$ must be specified, which depends on the operation mode. In the following, an operation mode is considered which is characterized by a freely definable path speed $V_P^{des}(t)$. In the general case of a path without natural parameterization, the path parameter derivatives $\dot{\zeta}$ and $\ddot{\zeta}$ have to be adapted continuously to achieve the desired path speed $\|\mathbf{v}_P\|\,\lambda = V_P^{des}(t)$, where $\lambda \in \{-1, 1\}$ specifies the flying direction along the path, i.e., $\lambda = \mathrm{sgn}\left(V_P^{des}\right) = \mathrm{sgn}\left(\dot{\zeta}\right)$. According to the desired path position $\mathbf{r}_P = \boldsymbol{\sigma}(\zeta)$, the desired path speed

follows as $\|\mathbf{v}_P\|\,\lambda = \|\boldsymbol{\sigma}'(\zeta)\|\,\dot{\zeta}$ and thus

$$\dot{\zeta} = \frac{V_P^{des}(t)}{\|\boldsymbol{\sigma}'(\zeta)\|} \quad (26a)$$

$$\mathbf{v}_P = \frac{\boldsymbol{\sigma}'(\zeta)}{\|\boldsymbol{\sigma}'(\zeta)\|}V_P^{des}(t) \ . \quad (26b)$$

For the thereby specified path parameter speed $\dot{\zeta}$ and with the desired path acceleration $A_P^{des}(t) = \dot{V}_P^{des}(t)$, the path parameter acceleration follows in the form

$$\ddot{\zeta} = \frac{A_P^{des}(t)}{\|\boldsymbol{\sigma}'(\zeta)\|} - \frac{(\boldsymbol{\sigma}'(\zeta))^{\mathrm{T}}\,\boldsymbol{\sigma}''(\zeta)}{\|\boldsymbol{\sigma}'(\zeta)\|^2}\dot{\zeta}^2 \ . \quad (26c)$$

From these quantities the desired acceleration $\mathbf{a}_P = \frac{\mathrm{d}^2}{\mathrm{d}t^2}\mathbf{r}_P$ can be calculated as

$$\mathbf{a}_P = \boldsymbol{\sigma}''(\zeta)\,\dot{\zeta}^2 + \boldsymbol{\sigma}'(\zeta)\,\ddot{\zeta} \ . \quad (26d)$$

If $\boldsymbol{\sigma}(\zeta)$ is two times continuously differentiable and $V_P^{des}(t)$ is continuously differentiable, i.e., $\boldsymbol{\sigma}''(\zeta)$ and $A_P^{des}(t)$ are continuous, also $\mathbf{a}_P$ results to be continuous. For the case of a natural parameterization, the relations $(\boldsymbol{\sigma}'(\zeta))^{\mathrm{T}}\,\boldsymbol{\sigma}'(\zeta) = 1$ and therefore $(\boldsymbol{\sigma}'(\zeta))^{\mathrm{T}}\,\boldsymbol{\sigma}''(\zeta) = 0$ hold. Thus, $\dot{\zeta}$ and $\ddot{\zeta}$ in (26) are reduced to

$$\dot{\zeta} = V_P^{des}(t) \quad (27a)$$

$$\ddot{\zeta} = A_P^{des}(t) \ . \quad (27b)$$

Finally, ζ, $\dot{\zeta}$, and $\ddot{\zeta}$ are inserted into the PFC law (24) to calculate $\mathbf{u}$ for a given path $\boldsymbol{\sigma}(\zeta)$. To further determine the desired quantities of the inner loop controllers in Section 3, $\mathbf{u}$ is transformed by means of (6) and (8).

The operation mode to fly with a definable path speed $V_P^{des}(t)$ is achieved by choosing the path parameter ζ according to (26). For other operation modes, e.g., a desired airspeed $V_A^{des}(t)$ or a manual throttle setting δ_T, further considerations can be made to reduce the control law (24) to the orthogonal path error. Taking into account wind allows for operation modes which include combined requirements for path speed and airspeed.

Constraints within the PFC structure can be separated and addressed directly due to the hierarchical control structure. Firstly, the velocity of the aircraft is subject to limitations, like maximum airspeed, stall speed, and maximum climb and descent rates. Therefore, the aim is to restrict desired velocities to feasible values. To this end, based on (24) the desired input $\mathbf{u}$ is rewritten in the form

$$\mathbf{u} = \mathbf{a}_P + k_D\left(\mathbf{v}_P + \underbrace{\frac{k_P}{k_D}(\mathbf{r}_P - \mathbf{r}_I) - \frac{k_I}{k_D}\mathbf{e}_I}_{\Delta\mathbf{v}_P} - \mathbf{v}_I\right) \ . \quad (28)$$

Thus, the input $\mathbf{u}$ reads as

$$\mathbf{u} = \mathbf{a}_P + k_D\left(\mathbf{v}_I^{des} - \mathbf{v}_I\right) \quad (29a)$$

$$\mathbf{v}_I^{des} = \mathbf{v}_P + \Delta\mathbf{v}_P = \mathbf{v}_P + \frac{k_P}{k_D}(\mathbf{r}_P - \mathbf{r}_I) - \frac{k_I}{k_D}\mathbf{e}_I \quad (29b)$$

10

and can be interpreted as a proportional controller for velocity control. Using this representation, $\mathbf{v}_I^{des}$ can be limited by defining constraints for $\Delta\mathbf{v}_P$ as $\Delta\mathbf{v}_{P,max}$. Secondly, acceleration constraints correspond to $a_{xB,max}$, $a_{zB,max}$, and φ_{max} according to (5), or more generally to the feasible acceleration space. A simple implementation method to take these limitations into account are box constraints. More extensive use of the feasible acceleration space may be achieved by model based optimization techniques. Thirdly, the acceleration demand of the PFC corresponds to desired values of the inner loop controller, which finally are mapped to constrained control inputs. By limiting low-level control quantities like ω_{xB} and c_{zB} to feasible ranges in combination with anti-windup methods for the integral errors, constraints of the control inputs are taken into account.

Finally, the tuning parameters of the PFC are chosen by placing all three roots of the characteristic polynomial, $p(s) = s^3 + k_D s^2 + k_P s + k_I$, to $s_1 = s_2 = s_3 = -0.25$. Therefore, the derivative coefficient results in $k_D = -3s_1 = 0.75$, which approximately determines the bandwidth of the velocity feedback, cf. (29). This is a forth of the designed bandwidth of C_φ, which is the slowest controller involved in realizing $\mathbf{u}$, cf. Table 2. Therefore, the assumption for the PFC that the inner loop control is significantly faster is justified.

An overview of the overall multi-loop control concept and the related quantities is given in Figure 1, where the results of this section are combined with the results of Section 2, Section 3, and Section 4.

6. Flight tests

In the following, the developed control concept is evaluated in real flight conditions by use of an unmanned aerial vehicle. Out of various flight paths the results of a 3D lemniscate path and a circular path are presented for comparability with state-of-the-art PFC concepts in the literature.

6.1. UAV test platform

The fixed-wing aircraft used for validation of the PFC concept is a model of a Piper PA18 Super Cub (PKZ6875) with a span of 1300 mm. The technical specifications can be found in Table 3.

Figure 8 illustrates the position of the controller, the sensors and actuators. The flight controller (Pixhawk) is an integrated solution, which contains accelerometer (LSM303D), gyroscopes (L3GD20H), and altimeter (MS5611). It is placed inside the fuselage, close to the center of gravity to avoid parasitic accelerations due to angular movements. The GPS (u-blox NEO-7) and 3-axes digital compass (HMC5883L) module delivers GPS position and time data as well as 3D magnetic flux information. For best reception of the GPS signal, placing the module on the top face of the aircraft is endeavored. For the magnetic flux sensor, a spot of low magnetic interference is

Length	865	mm
Span	1300	mm
Empty weight	991	g
Battery weight	202	g
Flying weight	1193	g
Propeller dimensions	9x6	inch
BLDC motor constant	960	rpm/V
BLDC max. current	18	A
Battery voltage	11.1	V
Battery capacity	2400	mA h
Clean stall speed	8	m s^{-1}
Maximum cruise speed	20	m s^{-1}

Table 3: Technical specifications of the investigated model of a Piper PA18.

beneficial. Electromagnetic disturbances are caused by the BLDC-motor and -controller, which are positioned in the front part of the aircraft. Therefore, the GPS and compass module is placed at the rear part of the top face. The airspeed sensor (4525DO) is connected to a pitot-static tube, which is located at the left wing. The position is such that the tip of the tube protrudes from the boundary layer and is sufficiently in front of the wing before significant airflow deflection. The lateral position is chosen outside the propeller's slipstream, still not too far towards the wing tip to avoid coupling of angular movements.

The servo output signals Servo 1 to Servo 6 of the microcontroller are configured as inputs to the servo motors, which deflect the control surfaces, and PWM throttle input for the BLDC motor controller, as indicated in Figure 8. All control surfaces are configured to have a maximum deflection of about 25°. The input signals for elevator deflection δ_E and rudder deflection δ_R are directly used as the servo inputs for Servo 2 and Servo 4, respectively. For positive δ_E, Servo 2 moves up, for positive δ_R Servo 4 moves to the right. The input signal for aileron deflection δ_A actuates Servo 1 and Servo 6 in opposite directions. For positive δ_A, Servo 6 moves up and Servo 1 moves down. The input signal for flap deflection δ_F also actuates Servo 1 and Servo 6, and additionally Servo 5. For positive δ_F all three servos move down to the same extent. Thus, Servo 1 and Servo 6 are used as so called "flaperons", i. e., control surfaces, which are used as both, aileron and flaps. Therefore, the input for flap deflection δ_F influences the curvature of the whole wing, instead of only the middle part. This results in two favorable effects. Firstly, the achieved increase or decrease of lift is greater. Secondly, the parasitic effect of a pitching moment is reduced. The inputs $\delta_A, \delta_E, \delta_F, \delta_R$ are normalized to $[-1, 1]$, whereas δ_T is normalized to $[0, 1]$.

6.2. 3D Lemniscate

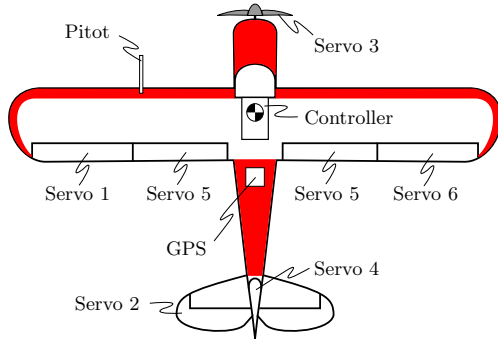The first validation path is a three-dimensional lemniscate, which is shown in Figure 9 together with the flight

Figure 8: Position of the flight controller, the sensors, and the actuators of the model of a Piper PA18.
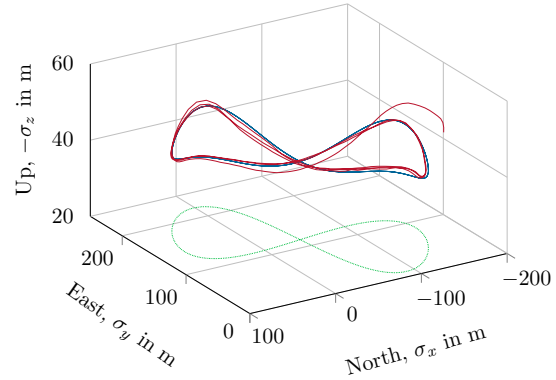

Figure 9: Path of 3D lemniscate (blue) with the trajectories of three rounds with an initial path error (red) and a 2D ground projection (green).

trajectory of three rounds including an initial path error. It is generated by

$$\boldsymbol{\sigma}_L(\zeta) = \begin{bmatrix} A_x \sin(2\zeta) \\ A_y (\cos(\zeta) - 1) \\ A_z (\cos(4\zeta) - 1) \end{bmatrix} \tag{30a}$$

$$\boldsymbol{\sigma}'_L(\zeta) = \begin{bmatrix} 2A_x \cos(2\zeta) \\ -A_y \sin(\zeta) \\ -4A_z \sin(4\zeta) \end{bmatrix} \tag{30b}$$

$$\boldsymbol{\sigma}''_L(\zeta) = \begin{bmatrix} -4A_x \sin(2\zeta) \\ -A_y \cos(\zeta) \\ -16A_z \cos(4\zeta) \end{bmatrix}, \tag{30c}$$

with $A_x = 60\,\text{m}$, $A_y = 120\,\text{m}$, and $A_z = 3\,\text{m}$. This results in a maximum climb gradient of $12.8\,\%$, which corresponds to a climb angle of $7.4°$. The path generating pattern (30) may be turned and tilted by means of a rotation matrix $\mathbf{R}_0$ and translated to a starting point $\boldsymbol{\sigma}_0$, i.e., $\boldsymbol{\sigma} = \boldsymbol{\sigma}_0 + \mathbf{R}_0 \boldsymbol{\sigma}_L$. In the case of Figure 9, the path is chosen to be aligned with the initial southeastern flight direction $\psi_0 = 126.8°$, i.e., $\mathbf{R}_0$ results as yaw rotation $\mathbf{R}_0 = \mathbf{R}_z(\psi_0)$. Furthermore, the initial position $\boldsymbol{\sigma}_0 = \begin{bmatrix} -141.1\,\text{m} & 44.3\,\text{m} & -40.5\,\text{m} \end{bmatrix}^\mathsf{T}$ is chosen such that an initial error of $\mathbf{e}_{P,0} = \begin{bmatrix} 10\,\text{m} & 10\,\text{m} & -10\,\text{m} \end{bmatrix}^\mathsf{T}$ occurs.

The 3D lemniscate path is used to validate the path following control for nonlinear three dimensional paths as well as for nonnatural parameterization. Figure 10 presents the path error of the first two rounds which are separated by the red dashed vertical line. The aircraft does not start on the path, but with an intended initial error of approximately $\mathbf{e}_{P,0} = \begin{bmatrix} 10\,\text{m} & 10\,\text{m} & -10\,\text{m} \end{bmatrix}^\mathsf{T}$, which can also be observed in Figure 9. The path error decays based on velocity restrictions $\Delta\mathbf{v}_{P,max} = \begin{bmatrix} 2\,\text{m s}^{-1} & 2\,\text{m s}^{-1} & 1\,\text{m s}^{-1} \end{bmatrix}^\mathsf{T}$, cf. (28). The errors $e_{P,x}$ and $e_{P,y}$ are close to zero after approximately $5\,\text{s} = \frac{10\,\text{m}}{2\,\text{m s}^{-1}}$, whereas $e_{P,z}$ is close to zero after $10\,\text{s} = \frac{10\,\text{m}}{1\,\text{m s}^{-1}}$. Thereafter, despite the highly dynamic path, a path error of less than $5\,\text{m}$ can be observed. The standard deviation of
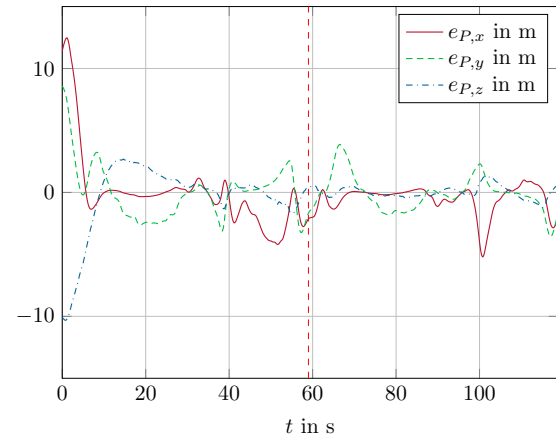

Figure 10: Path error of the first two rounds separated by the red dashed line with decaying initial path error.

$\|\mathbf{e}_P\|$ in the region from $10\,\text{s}$ until $119\,\text{s}$ is $1.61\,\text{m}$. To illustrate different methods of specifying the tangential motion along the path, Figure 11 shows the time evolution of the airspeed V_A and the inertial speed V_I together with the corresponding desired values V_A^{des} and V_P^{des} for the same test flight. The first round is flown at a desired airspeed $V_A^{des} = 13.2\,\text{m s}^{-1}$, which is realized by an airspeed controller. To this end, the PFC concept of Section 5 is extended by an algorithm to track the orthogonal path parameter and a modified control law, which is based on the orthogonal path error. The operation mode of the second round is identical to the one presented in Section 5. By including wind data by means of the relation $\mathbf{v}_I = \mathbf{v}_A + \mathbf{v}_W$, the desired path speed V_P^{des} is adjusted such that the airspeed stays in the range of $V_A^{des} = 13.2\,\text{m s}^{-1}$ also for the second round, cf. Figure 11. Choosing a constant desired path speed V_P^{des} would result in significant air-

12

speed variations, as the relative wind angle changes due to the varying flight direction in the course of the lemniscate path. The airspeed V_A in the second round results to deviate more from V_A^{des} than in the first round with the benefit of a smoother course of the inertial speed V_I. Such combined criteria for V_A and V_I can be of interest, e.g., as a trade-off between constant path speed V_P, which might be interesting for the air-traffic-control, and energy-optimal airspeed V_A, which might be interesting for the aircraft operator. To validate the functionality of the in-
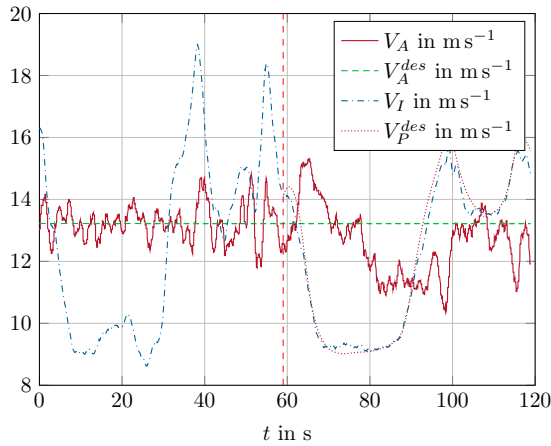

Figure 11: Comparison of flown airspeed V_A to desired airspeed V_A^{des} in round 1, and inertial speed V_I to desired path speed V_P^{des} in round 2.

ner loop, Figure 12 presents the three accelerations of (6), $\begin{bmatrix} a_{xB} & a_{zB,S} & a_{zB,C} \end{bmatrix}^{\mathrm{T}}$, and the resulting quantities φ and c_{zB} of the inner loop controllers. The desired values are tracked accurately, except for some lags of the φ control which subsequently generate deviations of the accelerations. Especially around 64 s, 98 s, and 115 s deviations due to the lower bandwidth of φ can be observed. These deviations correlate with the points of maximum path error in Figure 10. Comparing the performance of the PFC for strong turbulence with smooth air shows unchanged accuracy in tracking the path, i.e., disturbances are successfully suppressed. This is confirmed by Figure 13, which, in the upper plot, presents $\|\mathbf{e}_P\|$ for smooth and turbulent air conditions, i.e., the test flights were performed on different days. Still, the difference from smooth air to turbulent air can be found in the actuating variables, like δ_A and δ_F, which need to compensate disturbances in ω_{xB} and a_{zB}. In this context, Figure 13 compares the necessary control effort in smooth air to the control effort in turbulent air. Significantly larger deflections of δ_A, δ_E, and δ_F in turbulent air can be confirmed. Note that the elevator δ_E shows rapid deflections for dynamic δ_F deflections due to the high-pass characteristics of the filter $F_{\delta_F,\delta_E}^z(z)$, cf. Section 4. The rudder δ_R is designed for maintaining co-
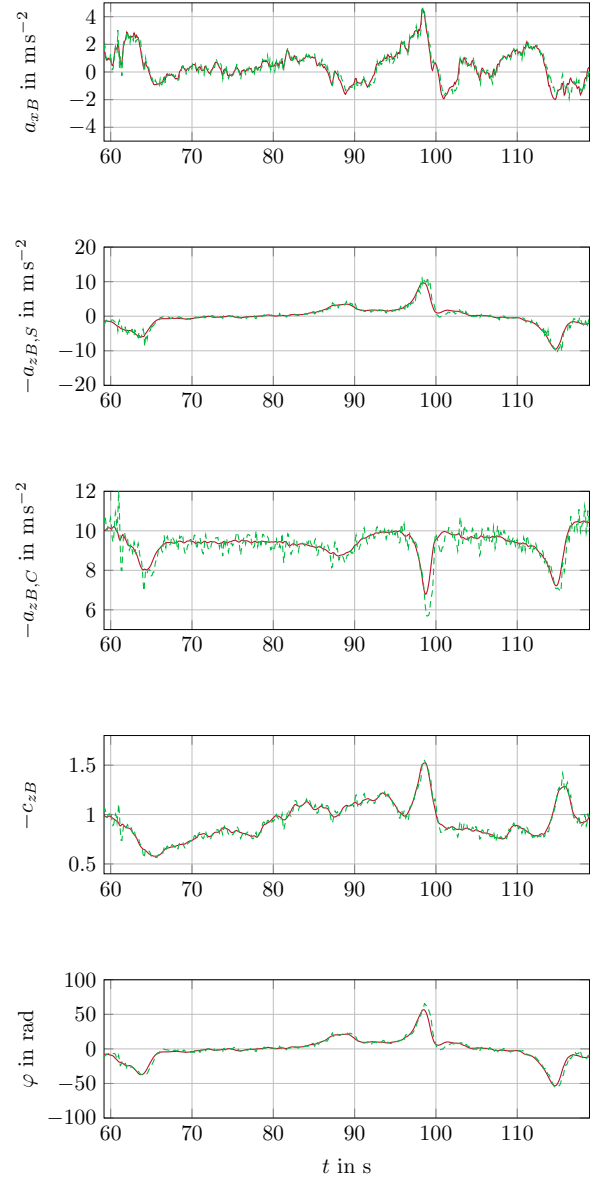

Figure 12: Comparison of desired (solid) and actual measured (dashed) quantities of the inner loop controllers: a_{xB}, $-a_{zB,S}$, $-a_{zB,C}$ and the resulting quantities $-c_{zB}$ and φ, cf. (8).

13

ordinated flight with low bandwidth, thus, high frequent turbulence shows only limited effect on the control effort. The trottle input δ_T is used to control the airspeed for the scenario of smooth air, as it is the case in the first round of Figure 11. For the test flight in turbulent air, an operation mode with direct δ_T input was chosen, i.e., the airspeed is not controlled but results according to an equilibrium state of thrust and drag. This is done due to the fact that rapid δ_T changes would be necessary to track the airspeed in turbulent air. Excessive δ_T variation is unwanted, as it causes heavy vibrations, which affect the acceleration measurements.

6.3. Circular Path

To allow for a comparison of the results with results from literature, cf. Section 1, three test flights with circular paths were performed. For the first two flights, smooth air was chosen, while the third flight was conducted under strong turbulent wind, i.e., gusts up to $20\,\mathrm{m\,s^{-1}}$.

The circle radius of the first flight is $R_1 = \frac{V_{ref}60\,\mathrm{s}}{2\pi} = 114.6\,\mathrm{m}$, i.e., at $V_{ref} = 12\,\mathrm{m\,s^{-1}}$ one round would take approximately $60\,\mathrm{s}$, half the time of a standard rate turn. Figure 14 shows a variety of flight states for validation and discussion of the results. Apparently, the first circle is flown with an airspeed of $V_A \approx 13\,\mathrm{m\,s^{-1}}$. The inertial speed $V_I \approx 15\,\mathrm{m\,s^{-1}}$ results to be even a little higher. Thus, one round is flown in $49.55\,\mathrm{s}$, less than $60\,\mathrm{s}$. For the special case of a circle, an almost constant lateral acceleration $-a_{zB,S} \approx 2\,\mathrm{m\,s^{-2}}$ results according to the centripetal acceleration $a_{CP} = \frac{V_I^2}{R_1} \approx 2\,\mathrm{m\,s^{-2}}$. For almost constant V_I, the time evolutions of the velocities $v_{I,x}$ and $v_{I,y}$, i.e., the inertial velocity components to the north and to the east direction, vary according to sine functions. The desired values $v_{I,x}^{des}$ and $v_{I,y}^{des}$ correspond to the representation (29). The yaw angle ψ which corresponds to the heading of the aircraft increases steadily. Without wind, the inertial flight direction $\psi_I = \mathrm{atan2}\left(\frac{v_{I,y}}{v_{I,x}}\right)$ corresponds to the in-air flight direction which is approximately the heading of the aircraft ψ. Indeed, ψ_I shows only little deviations from ψ. The derivatives $\dot{\psi}_I = \frac{\mathrm{d}\psi_I}{\mathrm{d}t}$ and $\dot{\psi} = \frac{\mathrm{d}\psi}{\mathrm{d}t}$ are approximately determined by means of a high-pass filter with $\omega_{HP} = 5\,\mathrm{rad\,s^{-1}}$. The turning rates show a mean value of approximately $\frac{360°}{50\,\mathrm{s}} = 7.2\,°\,\mathrm{s^{-1}}$. These values are used for comparison with the other two flights of circular paths. The main result of the first flight itself is the high path accuracy of under $50\,\mathrm{cm}$.

As the PFC concept is also designed for higher path dynamics, a considerably smaller radius of the circle $R_2 = \frac{V_{ref}12\,\mathrm{s}}{2\pi} = 22.9\,\mathrm{m}$ is chosen for the second flight. Additionally, the circle is flown with full throttle $\delta_T = 1$. Therefore, an airspeed of $V_A \approx 17\,\mathrm{m\,s^{-1}}$ results, as indicated in Figure 15. The inertial speed $V_I \approx 19\,\mathrm{m\,s^{-1}}$ results to be higher. A centripetal acceleration of $a_{CP} = \frac{V_I^2}{R_2} \approx 15\,\mathrm{m\,s^{-2}}$ is confirmed for $-a_{zB,S}$. This is significantly higher than the necessary centripetal acceleration for the first circle. Still, a path accuracy of mostly under $1\,\mathrm{m}$ with peaks up
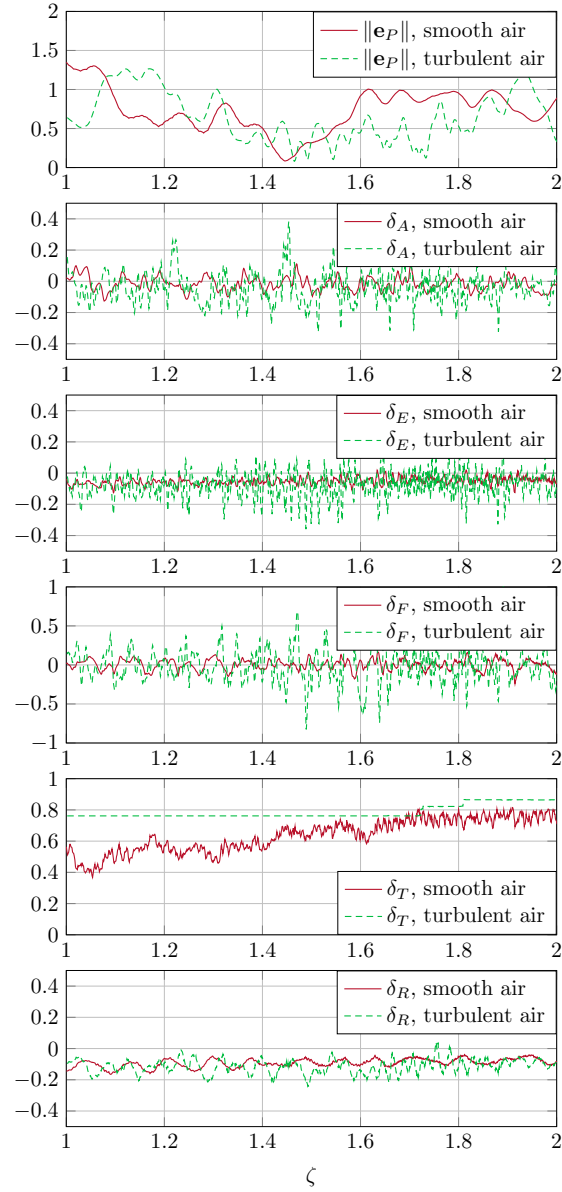

Figure 13: Comparison of $\|\mathbf{e}_P\|$, δ_A, δ_E, δ_F, δ_T, and δ_R for smooth and turbulent air.
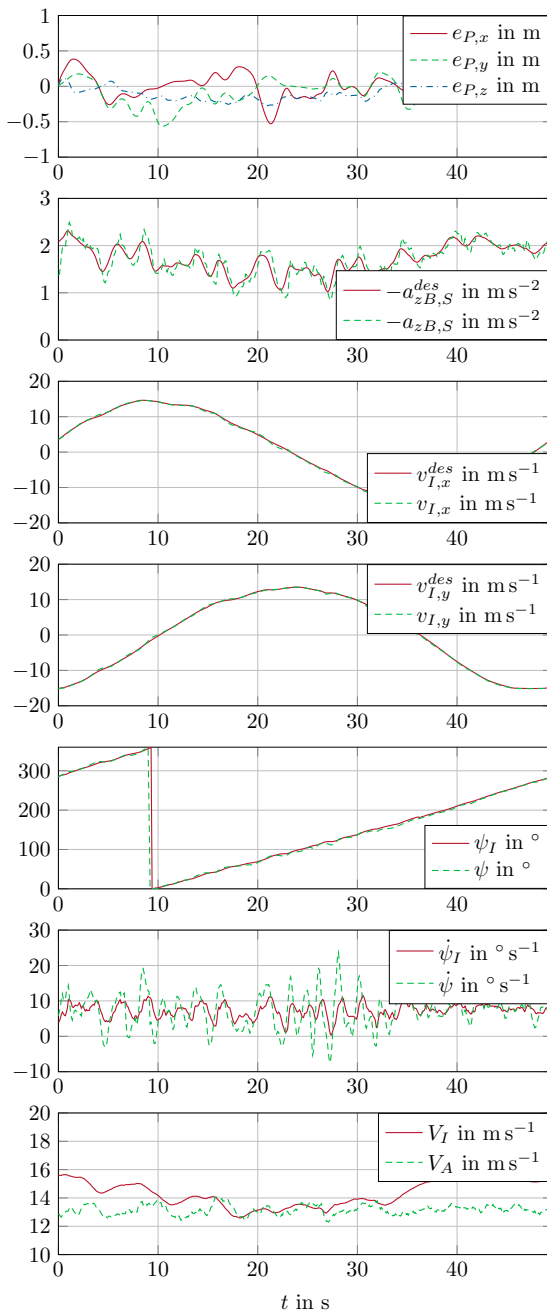
14

Figure 14: Values of path error $\mathbf{e}_P$, inner loop side acceleration $a_{zB,S}$, velocities $v_{I,x}$ and $v_{I,y}$, yaw angle ψ, yaw rate $\dot{\psi}$, inertial speed V_I, and airspeed V_A of a test flight in smooth air with a circular path of radius $R_1 = 114.6\,\mathrm{m}$.
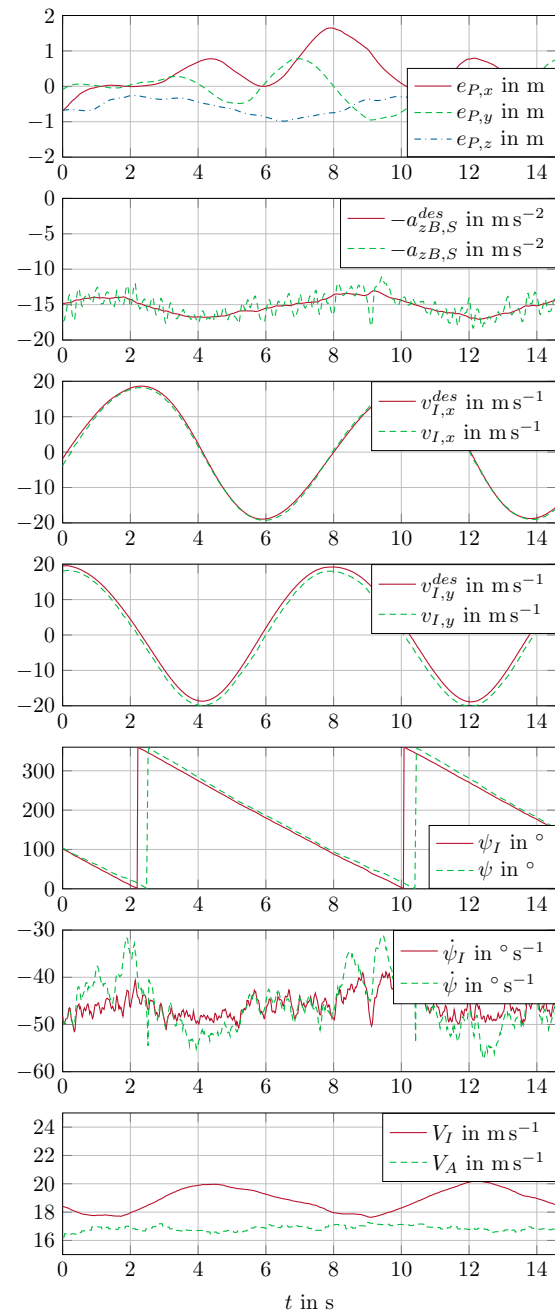
Figure 15: Values of path error $\mathbf{e}_P$, inner loop side acceleration $a_{zB,S}$, velocities $v_{I,x}$ and $v_{I,y}$, yaw angle ψ, yaw rate $\dot{\psi}$, inertial speed V_I, and airspeed V_A of a test flight in smooth air with a circular path of radius $R_2 = 22.9\,\mathrm{m}$.

15

to $2\,\mathrm{m}$ can be observed. In contrast to the first flight, $-a_{zB,S}$ results to be negative as the second flight is flown with negative path direction, which is also possible for the presented PFC concept. The velocities $v_{I,x}$ and $v_{I,y}$ again show sinusoidal characteristics. Due to the negative path direction ψ_I and ψ show a steady decrease, in contrast to the steady increase during the first flight. According to the smaller radius and therefore shorter lap time of approximately $8\,\mathrm{s}$, the absolute values of the turning rates $\dot\psi \approx \dot\psi_I$ yield $\left|\dot\psi_I\right| \approx \frac{360°}{8\,\mathrm{s}} \approx 45°\,\mathrm{s}^{-1}$. Due to $a_{CP} = \dot\psi_I V_I$, almost the same result is obtained by $\left|\dot\psi_I\right| = \frac{a_{CP}}{V_I} = \frac{15\,\mathrm{m\,s^{-2}}}{19\,\mathrm{m\,s^{-1}}}\frac{180°}{\pi\,\mathrm{rad}} = 45.2°\,\mathrm{s}^{-1}$. These values can be confirmed in Figure 15.

The last test flight is conducted with a circle radius like for the first flight, $R_3 = R_1 = 114.6\,\mathrm{m}$, but strong wind and turbulences. Figure 16 shows the recorded quantities of the third test flight. Gusts of up to $20\,\mathrm{m\,s^{-1}}$ require a sufficiently high airspeed $V_A \approx 19\,\mathrm{m\,s^{-1}}$ which is obtained by full throttle $\delta_T = 1$. Still, V_I almost gets zero at $63\,\mathrm{s}$. The velocities $v_{I,x}$ and $v_{I,y}$ do not show sinusoidal characteristics anymore, as V_I varies heavily. Also the downwind section from $36\,\mathrm{s}$ until $48\,\mathrm{s}$ takes significantly shorter time than the upwind section. Note that ψ and ψ_I do not show steady rise, but change a lot faster for the downwind segment. Furthermore, significant wind correction angles are necessary, i.e., ψ differs from ψ_I up to $40°$. The developed PFC concept does not control orientations but accelerations. Therefore, instead of calculating the correction angle, it results by the kinematic control. As the required centripetal acceleration a_{CP} depends on varying V_I, i.e., $a_{CP} = \frac{V_I^2}{R_3}$, it varies itself significantly. A peak of $8\,\mathrm{m\,s^{-2}}$ can be observed for the downwind segment, where $V_I \approx 30\,\mathrm{m\,s^{-1}}$, corresponding to $a_{CP} \approx \frac{(30\,\mathrm{m\,s^{-1}})^2}{R_3} \approx 7.8\,\mathrm{m\,s^{-2}}$. Despite the challenging flight conditions the path error only shows peaks up to $2\,\mathrm{m}$.

6.4. Discussion

By means of real test flights the performance of the presented PFC concept was examined. The PFC objectives *asymptotic convergence*, *invariance property*, and *tangential motion* are assessed by a decaying initial position error, the path tracking accuracy for different flight paths, and consideration of various operation modes.

For the highly dynamic 3D lemniscate path, a RMS path error of $1.61\,\mathrm{m}$ is observed in comparison to the RMS path error of $5.16\,\mathrm{m}$, which was achieved in Muniraj et al. (2017) for a less dynamic 2D lemniscate with about double the size of the lemniscate of this work. The test flights in Muniraj et al. (2017) are performed with a comparable airspeed of $15\,\mathrm{m\,s^{-1}}$. Furthermore, for a circular path with a radius of about $100\,\mathrm{m}$, the mean path error of $3.56\,\mathrm{m}$ is reduced to under $0.5\,\mathrm{m}$. To further improve the performance of the system, different error sources may be considered,
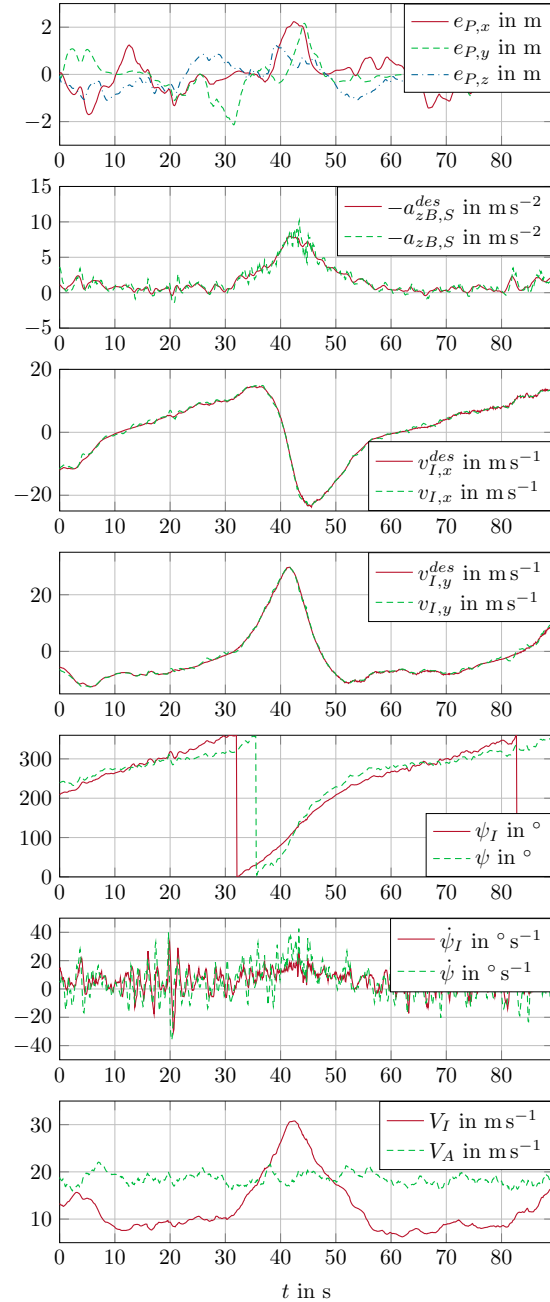

Figure 16: Values of path error $\mathbf{e}_P$, inner loop side acceleration $a_{zB,S}$, velocities $v_{I,x}$ and $v_{I,y}$, yaw angle ψ, yaw rate $\dot\psi$, inertial speed V_I, and airspeed V_A of a test flight with strong turbulent wind with a circular path of radius $R_3 = 114.6\,\mathrm{m}$.

16

as the overall path error is caused by the non-ideal generation of the necessary feedforward path acceleration $\mathbf{a}_P$, by the impact of disturbances, as well as by errors in the state estimation. The precision of the position, velocity, and attitude estimation with respect to the actual state of the aircraft directly influences the achievable path accuracy and may be improved by quality and quantity of sensors, as well as faster processing and optimization of the state estimation algorithm. For perfect state estimation, the path accuracy depends on the ability of the inner loop control to realize the demanded accelerations of the superordinate PFC. While longitudinal acceleration a_{xB} and vertical acceleration a_{zB} are generated by direct effects of thrust and direct lift control, lateral acceleration is generated indirectly by rotation of the lift force by means of a roll movement. The roll controller C_φ^z results to be of significant lower bandwidth than $C_{a_{xB}}^z$ and $C_{a_{zB}}^z$, cf., Table 2, and constitutes the limiting factor of the achievable dynamics of the feedforward path acceleration $\mathbf{a}_P$. To some extent the time evolution of $\mathbf{a}_P$ can be predicted by knowledge of the flight path, e.g., the zentripetal acceleration of an imminent curve. The inclusion of future path acceleration requirements, e.g., by MPC, may compensate for the settling time of the inner loop acceleration controller. For repetitive path segments, iterative learning control (ILC) also appears to be promising. Under the assumption that the inner loop control perfectly realizes the feedforward acceleration demand, the remaining path error source is given by gusts and turbulence. Analyzing the reaction of the presented control concept to changing wind, the following three cases can be distinguished for the example of straight and level flight:

- Headwind increases: The increased airspeed V_A causes an increase of $-a_{zB} = -c_{zB}\frac{V_A^2}{V_{ref}^2}a_{ref}$. However, c_{zB}^{des} instantaneously reacts for being calculated to $-c_{zB}^{des} = \frac{-a_{zB}^{des}}{a_{ref}}\frac{V_{ref}^2}{V_A^2}$, thus, decreases for increasing V_A and constant a_{zB}^{des}. The result is a fast upwards deflection of the flaps δ_F to decrease $-c_{zB}$ as the reference input $-c_{zB}^{des}$ does. A deflection of δ_E follows to return δ_F to its initial position. For an airspeed control, the increase of headwind acts as output disturbance. The desired value V_A^{des} is regained according to the dynamics of the airspeed controller. In case of V_P^{des} the higher airspeed would be kept, as the aircraft must fly faster for higher wind to maintain the same speed in the inertial frame.

- Crosswind increases: Side force corresponding to a_{yB} is generated due to a side slip angle. The aircraft itself is designed to turn into the new wind direction. The a_{yB} control additionally controls remaining deviations of a_{yB} to zero.

- Upwind increases: A change in vertical wind primarily changes the angle of attack. Therefore, c_{zB} changes, which acts as output disturbance to the c_{zB} control.

By initially deflecting the flaps, followed by an elevator deflection, the correct a_{zB} is regained.

As disturbances due to turbulence first of all alter accelerations, the inner loop already reacts before position errors occur. This can be also confirmed by test flights in heavy winds and turbulent air, where superior disturbance rejection is observed. Direct lift control allows to raise the bandwidth of the vertical acceleration control to 15 rad/s, i.e., to more than the double of 7 rad/s, which would be achievable with classical indirect lift generation solely by elevator deflection. For higher frequencies, acceleration disturbances are expected to show only small effect on the position error due to the double integration. Still, suppressing undesired accelerations itself might be of interest for safety and comfort reasons. To this end, even faster reaction to output disturbances may be achieved by a faster system, i.e., faster actuation, processing, and sensing. To further improve the suppression of turbulence effects, a disturbance feedforward by measuring the air movement in front of the airplane appears promising.

During test flights with wind speeds close to the aircraft's airspeed, wind correction angles of up to 40° are observed, cf., Figure 16. This correction angle is not calculated explicitly, but results from the translational movement as part of the assumed stable zero dynamics, as stated in Section 2. Regarding input constraints the conclusion can be drawn that the restriction of accelerations is a more direct approach to the limitations of a fixed-wing aircraft than the restriction of course rates or yaw rates. The acceleration generated by lift depends on c_{zB} and the actual airspeed, which determines the dynamic pressure, cf. (4). In Figure 16, the airspeed and therefore the achievable maximum acceleration remains approximately constant. However, the inertial speed V_I significantly varies due to the high wind speed. With the relation $a_{CP} = \dot{\psi}_I V_I$, it follows that for approximately constant maximum a_{CP}, the achievable maximum turning rate $\dot{\psi}_I$ is indirectly proportional to the inertial speed V_I. This can be confirmed, as for segments with headwind very low inertial speed V_I occur, which result in high values of $\dot{\psi}_I$ for low values of a_{CP}. In this context, the most direct constraint is to restrict $-a_{zB}$ according to the achievable lift generation.

Finally, the complexity of the concept regarding implementation and putting into operation is discussed. The computational complexity is assessed to be low, as only matrix multiplications and linear controllers of low orders are required. For the system identification, no wind channel, lab set-up or additional sensors are needed, as the identification flights are performed with the final system set-up. Acceleration measurements, which are essential for the inner loop control, are standard sensors for autopilot systems, as they are also necessary for the flight state estimation. The cascaded design of the PFC concept allows stepwise design and validation of the controller and putting them into operation independently.

7. Conclusions and Outlook

In this paper, a path following control (PFC) concept for fixed-wing aircraft was designed by incorporating the nonlinearities of the flight dynamics systematically.

In conclusion, the presented PFC concept is confirmed to be suitable for a wide range of nonlinear 3D paths. The performance is examined by means of real test flights with a model airplane, where an improvement to existing methods in literature regarding tracking performance and robustness to wind and turbulence effects is observed. To this end, the testing conditions are chosen similar to recent publications to allow for comparability. For low path dynamics, such as straight flight and constant rate turns of circles, a path error of less than $50\,\mathrm{cm}$ can be achieved. For high path dynamics, e.g., a change of desired side accelerations of $10\,\mathrm{m\,s^{-2}}$ in only $2\,\mathrm{s}$, cf. Figure 12, still, a path error of less than $5\,\mathrm{m}$, $1.61\,\mathrm{m}$ RMS, is achieved for a high dynamic 3D lemniscate path. To further assess advantages and drawbacks of different PFC methods, test flights including direct comparison of different PFC algorithms on various aircraft types would be necessary. The presented PFC concept appears beneficial also regarding the ease of implementation and computational complexity. The cascaded design facilitates the tuning and the placing into operation of the control system and allows to consider input constraints in accordance with the limitations of the fixed-wing aircraft. The transition from orientation to acceleration based inner loop control facilitates the feedforward of path accelerations, as well as corrections for wind effects. In this context, superior disturbance rejection is observed, as the acceleration control reacts even before position errors occur. By the use of direct lift control, the bandwidth of the vertical acceleration control is more than doubled.

Future work aims at further developing the control concept regarding tracking performance, disturbance rejection, and the adaption to other airframe types. In the context of current developments of manned and unmanned vertical take-off and landing (VTOL) aircraft, the PFC concept may be adapted for vertical flight and the transition between vertical and horizontal flight segments. To further improve the tracking performance, MPC and ILC can be considered to improve the calculation of feedforward path acceleration. For advanced disturbance rejection, faster feedback systems as well as disturbance feedforward of turbulence effects may be examined.

References

Aguiar, A.P., Hespanha, J.P., and Kokotović, P.V. (2008). Performance limitations in reference tracking and path following for nonlinear systems. *Automatica*, 44(3), 598–610.

Ahsun, U., Badar, T., Tahir, S., and Aldosari, S. (2015). Height control scheme without using pitch angle for fixed wing UAVs. *IFAC-PapersOnLine*, 48(9), 25 – 30.

Ardupilot (2018). Ardupilot open source autopilot software. `http://www.ardupilot.org/`. Accessed: 2018-10-17.

Bischof, B., Glück, T., and Kugi, A. (2017). Combined path following and compliance control for fully actuated rigid body systems in 3-d space. *IEEE Transactions on Control Systems Technology*, 25(5), 1750–1760.

Cichella, V., Kaminer, I., Dobrokhodov, V., Xargay, E., Hovakimyan, N., and Pascoal, A. (2011). Geometric 3D path-following control for a fixed-wing UAV on SO (3). In *AIAA Guidance, Navigation, and Control Conference*, 6415.

Di Francesco, G., D'Amato, E., and Mattei, M. (2015). Indi control with direct lift for a tilt rotor UAV. *IFAC-PapersOnLine*, 48(9), 156–161.

Franklin, G.F., Powell, J.D., and Workman, M.L. (1998). *Digital control of dynamic systems*, volume 3. Addison-wesley Menlo Park, CA.

Gates, D.J. (2010). Nonlinear path following method. *Journal of guidance, control, and dynamics*, 33(2), 321–332.

Isidori, A. (2013). *Nonlinear control systems*. Springer Science & Business Media.

Jaiswal, R., Shastry, A., Swarnkar, S., and Kothari, M. (2016). Adaptive longitudinal control of UAVs with direct lift control. *IFAC-PapersOnLine*, 49(1), 296–301.

L'Afflitto, A. (2017). *A Mathematical Perspective on Flight Dynamics and Control*. Springer.

Ljung, L. (1998). System identification. In *Signal analysis and prediction*, 163–173. Springer.

Lugo-Cárdenas, I., Salazar, S., and Lozano, R. (2017). Lyapunov based 3d path following kinematic controller for a fixed wing UAV. *IFAC-PapersOnLine*, 50(1), 15946–15951.

Merat, R. (2008). Study of a direct lift control system based on the A380 aircraft. In *46th AIAA Aerospace Sciences Meeting and Exhibit, Reno, NV*, 1432–1442.

Micaelli, A. and Samson, C. (1994). Trajectory tracking for two-steering-wheels mobile robots. *IFAC Proceedings Volumes*, 27(14), 249 – 256.

Mullen, J., Bailey, S.C., and Hoagg, J.B. (2016). Filtered dynamic inversion for altitude control of fixed-wing unmanned air vehicles. *Aerospace Science and Technology*, 54, 241–252.

Muniraj, D., Palframan, M.C., Guthrie, K.T., and Farhood, M. (2017). Path-following control of small fixed-wing unmanned aircraft systems with Hinf type performance. *Control Engineering Practice*, 67, 76–91.

Nelson, D.R., Barber, D.B., McLain, T.W., and Beard, R.W. (2007). Vector field path following for miniature air vehicles. *IEEE Transactions on Robotics*, 23(3), 519–529.

Nielsen, C., Fulford, C., and Maggiore, M. (2010). Path following using transverse feedback linearization: Application to a maglev positioning system. *Automatica*, 46(3), 585 – 590.

Park, S., Deyst, J., and How, J.P. (2007). Performance and lyapunov stability of a nonlinear path following guidance method. *Journal of Guidance, Control, and Dynamics*, 30(6), 1718–1728.

Pinsker, W.G. (1970). Direct lift control. *The Aeronautical Journal*, 74(718), 817–825.

Ratnoo, A., Sujit, P., and Kothari, M. (2011). Adaptive optimal path following for high wind flights. *IFAC Proceedings Volumes*, 44(1), 12985–12990. 18th IFAC World Congress.

Stengel, R.F. (2004). *Flight dynamics*. Princeton University Press.

Sujit, P., Saripalli, S., and Sousa, J.B. (2014). Unmanned aerial vehicle path following: A survey and analysis of algorithms for fixed-wing unmanned aerial vehicles. *IEEE Control Systems Magazine*, 34(1), 42–59.

Yang, K., Kang, Y., and Sukkarieh, S. (2013). Adaptive nonlinear model predictive path-following control for a fixed-wing unmanned aerial vehicle. *International Journal of Control, Automation and Systems*, 11(1), 65–74.